Florida State University Libraries

2016

Surface and Atmospheric Boundary Layer Responses to Diurnal Variations of Sea Surface Temperature in an NWP Model

Rachel R. (Rachel Rebecca) Weihs

Follow this and additional works at the FSU Digital Library. For more information, please contact lib-ir@fsu.edu

FLORIDA STATE UNIVERSITY

COLLEGE OF ARTS AND SCIENCES

SURFACE AND ATMOSPHERIC BOUNDARY LAYER RESPONSES TO DIURNAL VARIATIONS OF SEA SURFACE TEMPERATURE IN AN NWP MODEL

By

RACHEL R. WEIHS

A Dissertation submitted to the
Department of Earth, Ocean, and Atmsopheric Science
in partial fulfillment of the
requirements for the degree of
Doctor of Philosophy

2016

Copyright © 2016 Rachel R. Weihs. All Rights Reserved.

Rachel R. Weihs defended this dissertation on June 30, 2016.
The members of the supervisory committee were:

Mark Bourassa

Professor Directing Dissertation

Kristine Harper

University Representative

Vasubandhu Misra

Committee Member

Phillip Sura

Committee Member

Allan Clarke

Committee Member

The Graduate School has verified and approved the above-named committee members, and certifies that the dissertation has been approved in accordance with university requirements.

ACKNOWLEDGMENTS

This work would not have been possible if not for several important people to whom I would like to thank.

First, my advisor, Dr. Mark Bourassa. He has given me the opportunities of a lifetime. He has allowed to me travel and present at conferences in places I never thought I would be able to visit. He has recruited me for or helped me attain several professional work opportunities that are invaluable to my professional career. And he has exhibited the utmost patience while providing the guidance and encouragement when I needed it most.

I would like to thank my family. Without their support, I certainly would have never made it as far as I have. I owe them everything.

I want to thank Jorge Vazquez and Dimitris Menemenlis at the NASA Jet Propulsion Laboratory for their guidance and mentorship.

I would like to thank all the staff as well as past and present COAPS-ians that I have had the pleasure of working with over the last 8 years.

And, finally, I need to acknowledge all the friends I have made in Tallahassee, especially for their support and encouragement.

This work was supported through the NASA grant NNZ15AD45G, JPL/NASA grant 1419699, and JPL's Physical Oceanography Distributed Active Archive Center (PO.DAAC) summer internship program.

TABLE OF CONTENTS

List of Figures v

Abstract ix

1 Introduction **1**

2 Background on Diurnal Warming Structure **7**

3 Model Configurations and Data **9**
3.1 WRF Configuration 9
3.2 Skin Temperature Algorithm 11
3.3 SST Boundary/Initial Conditions 12

4 Two-way Coupled Simulation Comparisons **13**
4.1 Synoptic Conditions 13
4.2 Modeled Diurnal Warming and Near-surface Variability 13

5 Evaluation of SST and Wind Changes **26**

6 Near-surface Wind Field Responses **34**
6.1 Composite Wind Changes 35
6.2 Momentum Budget of Trajectories 39

7 One-way Versus Two-way Coupling on the Diurnal Cycle of SSTs **54**

8 Conclusions and Discussion **61**
8.1 Summary 61
8.2 Future Work 63

Bibliography 64

Biographical Sketch 71

LIST OF FIGURES

3.1 WRF-ARW model domain outlined by the bold box. 10

4.1 Wind speed (m/s, colored vectors), surface pressure, (mb, dashed contours), and magnitude of diurnal warming of SST (K, gray, solid contours) each day at 17Z for the week of 7-14 July, 2014. 14

4.2 Same as 4.1 for 17Z, 1-8 August, 2012 15

4.3 Time series of (top) magnitude of diurnal warming (K, light blue), wind speeds (m/s) for the diurnal (green) and daily-constant run (black), and incident surface solar radiative flux (W/m^2, red) at the grid point located 34°N, 51°W. Dark shaded areas represent nighttime hours for this particular location. 16

4.4 Magnitude of diurnal warming (K) (shaded) and the wind difference vector between the diurnal warming minus the daily constant run for 7 July at 13Z (top left), 15Z (top center), 17Z (top right), 19Z (bottom left), 21Z (bottom center), and 23Z (bottom right). 18

4.5 Probability density function of the magnitudes of diurnal warming for the July simulation (blue dashed line) and the August simulation (red solid line). 19

4.6 Mean differences in (top row) diurnal warming (K), (second row) air temperature at 1000 mb (K), (third row) pressure (mb), and (bottom row) wind speed (m/s) of the 7-day simulation for 7-14 July, 2014 (left column) and 1-8 August, 2012 (right column). The mean magnitude of diurnal warming (K) is plotted on the wind speed differences for reference. 20

4.7 Mean sea level pressure differences (top) and approximate minimum pressure locations (bottom) for a storm between dSST simulation (purple) and the daily-constant simulation (red). The pressure differences are averaged over 23Z 11 July and 10Z 12 July and the position of the storms are from 13Z 11 July to 5Z 13 July. 21

4.8 3-dimensional surface of the +1K atmospheric temperature anomaly at 23Z (24th hour of simulation) on (top left) 7 July, (top right) 8 July, (bottom left) 9 July, and 10 July. The diurnal warming magnitude (K) is contoured in black. 23

4.9 Diurnal warming magnitude (K, top left), difference in wind speed (m/s, top right) wind vectors from the diurnally varying simulation, averaged upward velocity between 1000 mb to 800 mb (m/s, bottom left) and outgoing longwave radiation (W/m^2, bottom right) at 19Z 8 July, 2014. The magnitude of diurnal warming (K) is contoured. 24

5.1 (Top) Time series of modeled skin SST (K) from the ZB algorithm (solid green), MUR foundation SST (dashed black), SEVIRI skin SSTs (red circles), and GOES skin

SST (blue triangles). (Four panels) Comparisons of a) MUR foundation vs SEVIRI skin SST, b) MUR foundation vs GOES skin SST, c) ZB modeled skin vs SEVIRI skin SSTs, and d) ZB modeled skin vs GOES skin SSTs. For figures b and d, only GOES data points where SEVIRI data exist are used. The mean bias is calculated by subtracting the y-axis SST from the geostationary data. 30

5.2 Comparisons of (top left) MUR foundation SSTs vs nighttime only GOES skin (K), and (top right) nighttime only data from ZB modeled SSTs vs nighttime only GOES skin SST (K), (bottom left) MUR foundation SSTs vs daytime only GOES skin SST (K), and (bottom right) daytime only ZB modeled SSTs vs daytime only GOES skin SST (K). 31

5.3 Boxplot distribution of the differences in SST (GOES-WRF) (K) (left axis) and the probability density of GOES SST sampling (light blue solid line) (right axis) as a function of Greenwich Mean Time. The boxes represent the 25th and 75th quartiles and the whiskers represent a 95% confidence level. 32

5.4 Comparisons of (left) wind speeds from the daily-constant simulation vs ASCAT-A (m/s) and (right) modeled wind speeds from the diurnally varying simulation vs ASCAT-A for the July simulation. Shaded values indicate the data density of the scattered data. 33

6.1 Mean differences in wind stress curl (left column) (N/m3) and surface wind divergence (right column) (1/s) over 7-14 July, 2014 (top row) and 1-8 August, 2012. The average magnitude of diurnal warming is contoured and mean wind vectors from the diurnally varying simulation are shown. 43

6.2 Probability distribution functions of the projected wind vectors onto the (left) k $\times$ dSST gradient vector and (right) along dSST gradient vector. For the probability distribution functions plotted on the left, the solid line represents the distribution of the cross-dSST gradient vector when the along-gradient vector component is approximately zero, the long dashed line is when the along-gradient component is negative, and the short dashed line is when the along-gradient component is positive. The same is true for the right figure when the along and cross-gradient vector components are interchanged. 44

6.3 (Top Panels) Box plots showing the changing distribution of wind speeds (m/s) as a function of lag from 16Z on 7 July, 2014. A lag time $t = -6$ means the wind speed differences from 10Z are plotted relative to the locations of the diurnal warming gradient occurring at 16Z. The box plots are binned by the magnitude of directional derivative (magnitude of the wind in the direction of the dSST-gradient) from ocean warming occurring at 16Z. The length of the boxes indicates the magnitude of the 25th and 75th quartiles, the red line inside the box is the median value. The green line is the slope of a line fitted to medians of the first and last six boxes of the plot. (Bottom plot) The magnitude of the slope as a function of lag time. 45

6.4 Tendency of wind-dSST coupling as a function of time after diurnal warming has occurred on each day of the simulation from lags = 0 to 10 hr. Each segment represents the slope of the line fitted to the median of the wind speed distribution (see Figure 6.3) as a function of hour after the initial time (red triangles). The initial time represents the time at which the directional derivatives were calculated. For clarity, the first segment plotted here is the replication of a portion of the slop tendency plotted in Figure 6.3. 46

6.5 Mean (top row) anomaly time series and (bottom row) wavelet power spectra of the (left) magnitude of diurnal warming (K), (middle) sea level pressure (hPa) difference, and (right) wind speed difference (m/s) between the diurnally varying and daily-constant simulations for 1-8 August, 2012. 46

6.6 Same as Figure 6.5 for wind differences (m/s) that have been spatially filtered to reduce variability with wavelengths smaller than (left) 2°, (middle) 3°, and (right) 4° latitude and longitude. 47

6.7 Hovmöller diagram of the diurnal warming (contours, K) and differences in wind speed (shaded, m/s) and wind vectors occurring in the diurnally-varying simulation for the 1-8 August case study at 32°N. 48

6.8 (Left) positions of surface-based trajectories as a function of hour into the July 2014 simulation over contoured diurnal warming greater than 0.5 K and (Right) the changes in wind speed (shaded), vector wind difference (m/s), and the magnitude of diurnal warming (K) (contoured every 0.25 K) at 01Z 8 July. 49

6.9 (Right top) Mean amplitude of the diurnal warming (K, blue line) and wind speed difference (m/s, black line) between the diurnally varying and daily-constant trajectories. (Left column) Values in the daily-constant simulation and (right column) differences between daily-constant and diurnally varying simulations in the U (m/s) (second row), V (m/s) (third row), and W (mm/s) (fourth row) components of the wind vector within the lowest 2 km for trajectories in Figure 6.8 50

6.10 Differences in the terms of the marine boundary layer momentum budget; a) along-wind advective tendency, b) along-wind vertical advection, c) along-wind turbulent stress divergence, d) along-wind pressure gradient force, e) cross-wind advective tendency, f) cross-wind vertical advection, g) cross-wind turbulent stress divergence, h) cross-wind pressure gradient force, and i) Coriolis force in units of m/s^2 for trajectories flowing across warm to cooler dSST. The average time series magnitude of diurnal warming (K) is plotted in the bottom row for reference. 51

6.11 Same as Figure 6.9 for trajectories flowing from warmer to cooler SST 52

6.12 Same as Figure 6.10 for trajectories flowing from warmer to cooler SST. 53

7.1 Mean diurnal warming (K) for the one-way (red line) and two-way (green line) coupled WRF simulation for 7-14 July, 2014. 56

7.2 One-way minus two-way coupled differences in wind speed (m/s) at peak diurnal warming versus one-way minus two-way coupled peak diurnal warming (K) for the July simulation. The shaded values indicate data density of the scattered data. 58

7.3 One-way minus two-way coupled differences in the amplitude of diurnal warming (K) at 19Z 7 July (top left), 21Z 7 July (top middle), 23Z 07 July (top right), 1Z 8 July (bottom left), 3Z 8 July (bottom middle), and 5Z 8 July (bottom right). 59

7.4 One-way minus two-way coupled differences in the latent heat flux (W/m^2) at 19Z 7 July (top left), 21Z 7 July (top middle), 23Z 07 July (top right), 1Z 8 July (bottom left), 3Z 8 July (bottom middle), and 5Z 8 July (bottom right). 60

ABSTRACT

An atmospheric model is coupled to a sea surface temperature algorithm that calculates the diurnal variability in order to understand the responses to near surface winds and boundary layer temperature, pressure, and moisture in the north Central Atlantic. 7-day case study simulations with diurnally varying sea surface temperatures and daily-constant sea surface temperatures are compared. With the inclusion of diurnal heating during the day, the local heat fluxes are increased and the surface pressure decreases. The extent of the surface-induced heating to the atmosphere is not necessarily restricted to the boundary layer depending on the atmospheric stability and the interaction with synoptic scale weather. The diurnal variations in sea surface temperature also induce positive and negative mean wind speed anomalies on the order of 0.5 m/s over the 7-day period. Hourly changes to the wind field, however, can exceed 3 m/s particularly where modifications to the regional weather occur. A comparison to geostationary data show that the sea surface temperature algorithm overestimates the warming on average, but this overestimation could be exaggerated from several factors including smoothing of the geostationary data.

We examine the spatial variability and data distribution of the wind field anomalies in response to the diurnal sea surface temperature gradients at hourly and daily time scales. The changes to the wind field on the first day of diurnal warming exhibit a linear, but temporally lagged response to the direction in which flow crosses the diurnal warming gradient. This trend was also observed on day 2, but does not exist for subsequent days after. It is thought that the larger amplitude responses of interaction with the synoptic scale (secondary feedbacks) dominate the distribution for areas in which we expect wind-sea surface temperature coupling. The surface pressure gradient and Coriolis are deemed the dominant forcing processes in the model that generate the initial wind-diurnal sea surface temperature coupling response on the first day of the simulation.

In order to understand the importance of interactive feedbacks of the wind and the diurnal cycle of sea surface temperatures, we compared the duration and amplitude of the diurnal warming produced in a one-way coupled simulation. The one-way coupled simulation allows the diurnal variations in sea surface temperature to influence the surface fluxes at the concurrent time step, but uses winds from a non-diurnally modified SST to calculate the diurnal warming of the sea surface temperature. As compared to two-way coupled simulations, the mean amplitude of the

diurnal warming is larger and the duration is longer. This is one way to demonstrate that the integrated hourly feedbacks to the diurnal variability of sea surface temperature are important in producing an accurate duration and amplitude of diurnal heating over the day.

CHAPTER 1

INTRODUCTION

Sea surface temperature (SST) spatial and temporal variations have long since been known as vital components of earth's climate system. Discoveries of synoptic and/or mesoscale (such as eddies and ocean fronts) and their subsequent effects on the boundary layer are a major focus of current research [e.g. *Wai and Stage*, 1989; *Hashizume et al.*, 2002; *Small et al.*, 2008; *Back and Bretherton*, 2009; *O'Neill et al.*, 2010]. The highest resolution and most accurate SST products are needed for such studies. Understanding SST variability has helped the scientific community learn about global to regional scale climate variability. For example, the El-Nino Southern Oscillation (ENSO) and its associated temperature anomalies in the Tropical Eastern Pacific have been linked to changes in precipitation in the Western Pacific [e.g. *Clarke*, 2008], wind shear changes in the tropical Atlantic [e.g. *Goldenberg and Shapiro*, 1996; *Aiyyer and Thorncroft*, 2006], jet stream changes over the continental U.S., and shifts in seasonal storm tracks in the Southeastern U.S [e.g. *Alexander et al.*, 2002; *Eichler and Higgins*, 2006]. Numerical weather prediction (NWP) models are commonly forced with daily or monthly SSTs under the assumption that they contain enough of the intraseasonal or seasonal variability to produce these important climate processes within the models [*Noh et al.*, 2011]. In recent literature, however, more emphasis has been placed on the high frequency, diurnal variability of SSTs and the role it plays in the longer term climate [*Fairall et al.*, 1996a; *Webster et al.*, 1996; *Bernie et al.*, 2005; *Shinoda*, 2005; *Bernie et al.*, 2007; *Clayson and Weitlich*, 2007; *Kennedy et al.*, 2007].

In the past, the observed diurnal changes in SSTs and their subsequent diurnal modifications of the boundary layer were considered relatively weak and could largely be neglected [*Sverdrup et al.*, 1942; *Chen and Houze*, 1997]. This is often the case when wind speeds are high (above 10 m/s, for instance) and turbulent mixing from the strong surface stress creates a well-mixed, daytime boundary layer in the upper ocean. With a well-mixed ocean boundary layer, the SST is more akin to a bulk or mixed layer SST [*Soloviev and Lukas*, 2006]. However, in conditions of light winds and ample solar radiation absorption, heat begins to accumulate and stratify the upper few

meters of the ocean. Without sufficient mixing, either from the surface or advection via other ocean dynamical processes, warming of SSTs over the course of the day can be >3 K [e.g. *Stramma et al.*, 1986; *Fairall et al.*, 1996b; *Soloviev and Lukas*, 1997; *Kawai and Wada*, 2007; *Brunke et al.*, 2008; *Gentemann et al.*, 2009; *Weihs and Bourassa*, 2014] to >5 K [e.g. *Gentemann et al.*, 2008; *Merchant et al.*, 2008; *Clayson and Bogdanoff*, 2013]. Diurnal warming of the upper ocean exhibits a strong, spatially coherent seasonality due to the variability of wind speed and incident solar radiation, and has been shown to occur over large regions of the ocean [e.g. *Webster et al.*, 1996; *Stuart-Menteth*, 2003; *Kennedy et al.*, 2007; *Gentemann et al.*, 2008; *Bellenger and Duvel*, 2009].

Heating of this amplitude induces changes in surface energy transfer between the ocean and the atmosphere and can be explained to a first order by hydrostatic balance and the Clausius-Clapeyron principle. When diurnal warming is present, it typically increases the surface heat fluxes [e.g. *Fairall et al.*, 1996b; *Webster et al.*, 1996; *Ward*, 2006; *Weihs and Bourassa*, 2014] as long is it is larger than the cooling effect of evaporation and molecular diffusion at the surface interface (on the average of about 0.3 K to 0.6 K [*Bellenger and Duvel*, 2009]). However, how this heat transfer from diurnal warming is distributed via modification of the marine atmospheric boundary layer is not fully understood. *Kawai and Wada* [2007] have tried to estimate this effect by studying the total atmospheric heat gain when incorporating diurnal warming over a three-day period using TRITON buoy data in the western Pacific. Most of this heat gain was observed in the latent heat flux. Though they determined that the amount of heat gain would only heat a 10-m-thick water column by 0.02 K, the heat capacity of air is much smaller and it could be enough to destabilize the lower atmosphere. Diurnal warming has also been closely linked to changes in tropical convection in the western Pacific warm pool [e.g. *Webster et al.*, 1996]. *Chen and Houze* [1997] proposed that, when looking at observations during the TOGA COARE ISO period, diurnal variations in the tropical ocean and subsequent atmospheric boundary layer may impact the life cycles of deep convective tropical complexes (initiating in the afternoon) and spatial day-to-day organization of these cloud systems. Specifically, after a strong convective event, the moist boundary layer is slow to recover and the local surface conditions responsible become less favorable (i.e. cooling from downdrafts and shading from residual upper-level cloud decks) for development of afternoon heated convection in the same location. Instead, convection develops in clear regions near the previous day's cluster (i.e. "spatial selective behavior"). Thus, deep tropical convection is

a complex system of surface and cloud-radiation dynamics. *Wei et al.* [2001] and *Woolnough et al.* [2000] showed that the inclusion of the diurnal cycle of SSTs better matches the observations of interannual variations of surface flux and precipitation, and SST, respectively. *Bernie et al.* [2005] showed that the intraseasonal SST variation decreases if the diurnal variations of the surface fluxes are neglected. These studies all suggest that diurnal variations in SST need to be taken into account in order to understand longer term SST and heat flux seasonal and climate-scale variability.

The implications of SST diurnal variability are important for data producers of, for example, multi-platform, cross-calibrated SST products. Often, newer satellite-derived SSTs are calibrated with in situ measurements that are typically taken at different depths. For instance, the microwave (infrared) wavelengths used by active (passive) sensors to detect SSTs penetrate (detect) the sea surface at depths of millimeters (microns) versus a buoy at 1 to 5 m depth. As mentioned previously, depending on the stratification in the upper ocean, the temperature bias between the two sources can be on the order of a few degrees. Similar errors are found when comparing multi-satellite observations at different times of the diurnal cycle [*Gentemann*, 2003; *Donlon et al.*, 2007]. If the cross-calibration techniques used do not carefully consider possible inhomogeneities of input SST data, estimations of uncertainty in SST used to determine the suitability of the data for a given application may not be accurately determined [*Donlon et al.*, 2007].

Gradients of SSTs are also closely linked to changes in wind speeds; as air is advected over warmer water, changes in the evaporation, moisture, and surface heat fluxes can destabilize the lower marine atmospheric boundary layer. According to *Chelton et al.* [2001], positive wind stress curl develops as a result of wind aloft blowing parallel to sea surface temperature isotherms due to horizontal wind shear along boundary currents. The wind shear is also a result of the acceleration of winds on the warm side of the SST gradient, creating wind divergence as the wind blows from cool to warmer waters. Two mechanisms are typically cited as drivers of air-sea coupling: 1) the baroclinic driven horizontal pressure perturbations induce a horizontal wind perturbation, and 2) the thermally and surface drag-induced vertical mixing of momentum down to the surface [e.g. *Wallace et al.*, 1989; *Liu et al.*, 2000; *Anderson*, 2001; *Chelton et al.*, 2001, 2004; *Chelton and Wentz*, 2005; *Chelton et al.*, 2007; *O'Neill*, 2012]. Changes in wind speed over an ocean front have been measured anywhere between 3 m/s [*Anderson*, 2001] and 5 m/s [*Sweet et al.*, 1981]. Many studies showing the coupled feedbacks of winds and SSTs demonstrate the effects near large SST

gradients on climatological features such as western boundary currents, tropical instability waves, or eddies [i.e. *Sweet et al.*, 1981; *Chelton et al.*, 2001, 2007]. Diurnal warming of SSTs, on the other hand, can produce a diurnal sea surface temperature gradient that can be of similar magnitude to these longer time scale sea surface temperature features. The SST-driven wind speed feedback is of great interest to diurnal warming studies not only because the initial wind speed is important for the development of heating in the upper ocean, but also because the heating may cause wind acceleration that could modify the latter portions of the diurnal cycle.

To summarize, the neglect of the short-term ocean surface and near surface atmospheric dynamics could produce measurable errors in the coupled ocean-atmosphere interactions on daily, monthly, and longer seasonal scales. According to *Kawai and Wada* [2007], "As of yet, we do not know the impact of the diurnal SST variation on physical properties or processes in the atmosphere, especially in the boundary layer." Recent studies, such as *Noh et al.* [2011] and *Bellenger and Duvel* [2009], have used coupled ocean or skin temperature and atmospheric models to quantify the impact of SST diurnal variability on the climatology of surface heat fluxes, upper ocean structure, and intraseasonal variability. However, they have not addressed the coupling between the diurnal variability of SSTs and winds on daily timescales, nor its impact on the larger mesoscale/synoptic scale. *Wang and Duan* [2012] used an atmospheric mesoscale model to study the SST cooling due to wind-driven ocean mixing, but this was done using a case study of a typhoon (high winds case). This study aims to produce new evidence of the impact diurnally varying SSTs have on the near-surface and atmospheric planetary boundary layer and identify the changes in wind speed and SST variability. This will be done using a coupled atmospheric and ocean surface heating model over the extratropical Atlantic Ocean. Coupling the atmosphere to the ocean information can improve the performance of the model by improving the simulation of surface fluxes particularly when heat transport by the ocean circulation is small [*Noh et al.*, 2011].

The goals of this study are to 1) understand the effect of diurnal SST variability on the modification of the the short-term, near-surface wind fields and atmospheric boundary layer in terms of surface heat fluxes, heat transport, and atmospheric motion; 2) determine whether a linear relationship exists between diurnally-produced SST gradients and changes in the wind field on diurnal time scales and whether these changes are consistent with the literature (i.e. wind divergence on warm side of an SST front); and 3) determine the role/importance of two-way (ocean to atmosphere

back to ocean) coupled wind changes to latter evolution of the diurnal cycle of SST. The first goal is a proof-of-concept to demonstrate that there is sufficient evidence that the SST fields are modifying/modified by the atmosphere on diurnal scales in the model. Our experiments are designed to further understand the boundary layer changes induced by diurnal warming, both locally and regionally in space and in time. We can view these changes in terms of surface pressure, cloud cover, atmospheric temperature, and surface heat fluxes. These changes could indicate how much of an impact diurnal warming would, for instance, have on adjacent (regional) mesoscale weather within the vicinity of diurnal warming. In turn, modifications to the energy transport (through stability changes) would modify near surface wind speeds and atmospheric wind speed profiles. Our second goal is to understand how these wind changes occur in response to diurnal warming.To our knowledge, this is the first study to investigate the impact of diurnally-produced SST gradients on wind speed changes on subdaily to daily time scales. This is important because changes in wind field and its derivatives (i.e.wind stress) have paramount consequences in, for example, changes in Ekman upwelling in the ocean, heat flux transfer into the atmosphere, and perhaps changes in atmospheric circulation. The third goal is of particular interest to future diurnal modeling studies, wherein the evolution of the diurnal wind pattern is studied compared to the evolution of heating in the upper ocean. In coupling the SST to surface fluxes, we can quantify the changes in wind speed in the early stages of diurnal warming development and how they will impact the latter portions of the diurnal cycle of the SST. Coupling the two-way perpetual feedbacks of SST and winds (as opposed to one-way coupled model where the diurnal SST impacts atmosphere only) will help determine the importance of this diurnally-induced wind feedback and whether it acts as a self-regulator to diurnal warming. If the associated wind "gustiness" is present over the diurnally warmed SSTs within the model simulations, we expect the overall diurnal warming magnitudes to be smaller in a coupled system than without. Currently, most diurnal warming models parameterize the baroclinic and/or stability changes induced wind gustiness in times of very low wind speeds [*Fairall et al.*, 1996a]. The atmospheric model description and configurations used in this study are given in Chapter 3.1. Sea surface temperatures are updated to the atmospheric model via a skin algorithm that is described in Chapter 3.2. We will discuss the changes of surface pressure, air temperature, and cloud cover with the presence of diurnal variability (Chapter 4) as well as the near-surface winds and their responses in time and space in relation to diurnal warming (Chapter 6). Evaluation of

the magnitude of the diurnal warming and wind speeds are given in Chapter 5. Finally, we will compare the production of diurnal warming and the overall cycle shape and duration with simulations wherein two-way feedbacks (SST modifies atmosphere and modified atmospheric forcings are used for subsequent time steps) and one-way feedbacks (diurnally heated SST simultaneously modifies atmosphere only but fluxes and winds computed from a nighttime SST are used for to compute the diurnal warming) are allowed (Chapter 7). A summary and discussion is presented last in Chapter 8.

CHAPTER 2

BACKGROUND ON DIURNAL WARMING STRUCTURE

The dominant feature of diurnal warming within the vertical profile is the warm layer in which thermal stratification of the upper few meters is created by solar radiation absorption and small or nonexistent vertical mixing from low wind speeds [*Donlon et al.*, 2007; *Kawai and Wada*, 2007; *Bellenger and Duvel*, 2009]. The warm layer can either be visible via its own diurnal mixed layer or be incorporated into a diurnal thermocline which separates the warm layer from the mixed layer beneath it [*Soloviev and Lukas*, 2006]. At the very surface to within 0.1-1 mm depth, the temperature can be several tenths cooler via evaporation (or more specifically, molecular diffusion) and thus it is aptly named the cool-skin layer [*Kawai and Wada*, 2007]. Cooling of the skin layer is approximately 0.3 K on average [*Bellenger and Duvel*, 2009]. However, the cool-skin effect can be reduced by, for example, significant warming below, or when hot air temperatures are warmer than that of the water [*Kawai and Wada*, 2007], or wave-induced mixing. The upper ocean structure can be described as one-dimensional, with 1) a cool-skin at the very surface of the ocean (herein referred to as cool-skin SST) due to surface evaporation, 2) a shallow, diurnal mixed layer that retains most of the solar radiant heating (but possibly mixed from salinity gradients and/or surface waves), and 3) a mixed layer ocean below that [e.g. *Price et al.*, 1986; *Soloviev and Lukas*, 2006; *Donlon et al.*, 2007; *Kawai and Wada*, 2007]. Because we can neglect horizontal effects, we need only consider local surface inputs as forcing for the heating of the upper ocean. It is worth nothing that some evidence exists to suggest that diurnal warming is also subject to tides [*Price et al.*, 1986], but this effect was not addressed in this study.

Another key component is the temporal variability of the sea surface temperature with respect to the upper ocean buoyancy fluxes. Depending on the wind conditions and cloud cover, diurnal warming typically peaks in late afternoon after the peak incoming solar radiation—or more specifically, the time in which the net near surface energy flux is zero (after heating). The temperature begins to cool as the positive buoyancy forces from the volume absorption of the solar energy are

weakened and the convective/shear-driven turbulence becomes larger [*Soloviev and Lukas*, 2006]. Typically, nighttime oceanic convection overturns the surface water, and SST decreases close to that of a mixed-layer temperature or nighttime minimum [*Bellenger and Duvel*, 2009]. In some cases, as this study will demonstrate, the minimum occurs shortly after sunrise because the strong diurnal warm layer has not been completely entrained overnight.

CHAPTER 3

MODEL CONFIGURATIONS AND DATA

3.1 WRF Configuration

The Weather and Research Forecasting (WRF-ARW) Model [*Skamarock et al.*, 2008] is an atmospheric numerical weather prediction model that can be used to study different synoptic and/or mesoscale features in the atmosphere with fully compressible, non-hydrostatic Eulerian equations. WRF allows the user to modify many features, including a variety of physics packages, in order to test surface flux and boundary layer schemes, for example. Most importantly for this research, it can ingest SST information and beginning in version 3.5, the skin SST (or the temperature at which the atmosphere actually "sees") can be updated via a built-in SST algorithm. The SSTs are assimilated into the system via the surface heat fluxes.

This model is used to compare two simulations, with and without diurnal variability in the SSTs, for a variety of case studies. For each case study, the first simulation is the diurnally varying run in which the SST is updated each time step by an incorporated skin SST algorithm and the skin SST is sent to the surface flux routines. The reference run (herein referred to as the daily-constant run) uses a foundation SST (defined as the SST that is unaffected by diurnal variability [*Donlon et al.*, 2007]). Using a foundation SST as input to the model represents ocean forcing that does not explicitly contain both diurnal heating and cool-skin effects. The foundation temperature still retains longer time scale (seasonal) trends and is akin to models forced by climatology SSTs. The advantage of using foundation temperature is to understand the wholistic impact of diurnal warming (that is, the impact of the full magnitude of diurnal warming) as opposed to using a daily mean. We should note, however, that it may be possible that some small artifact of diurnal warming may be unintentionally superimposed onto the foundation temperature. For instance, the nighttime SST may be affected if the diurnal warming occurring in the real world is not eroded completely overnight. Estimating this impact is elusive because the information necessary to determine the impact is circular; we need a foundation temperature to determine the diurnal warming but the warming can impact the foundation temperature.

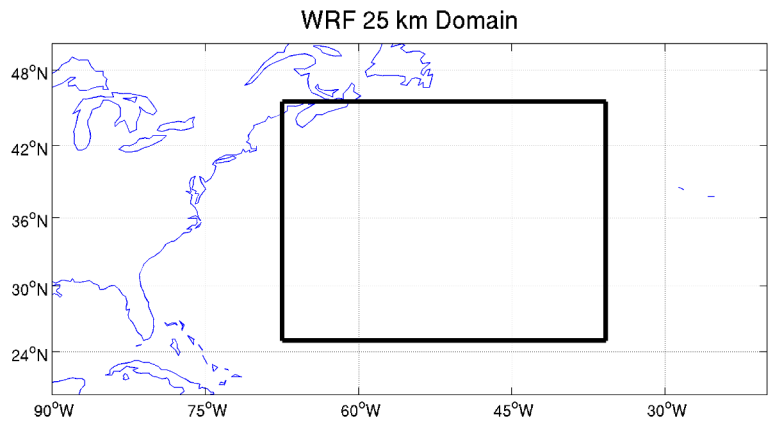

Figure 3.1: WRF-ARW model domain outlined by the bold box.

Unless otherwise noted, the results in this paper focus on the week-long simulations conducted over July 7-14, 2014 and August 1-8, 2012. All experiments were conducted for a large portion of the central northern Atlantic basin from approximately 72.46°W to 35.78°W, 25.03°N to 45.54°N on a 25 km scale with 60 vertical levels (Figure 3.1). This domain and time period are chosen on the basis that diurnal warming events frequently occur in this area during boreal summer [see *Weihs and Bourassa*, 2014, fig. 6]. Furthermore, during this time period, we find physically appropriate conditions that are both generally optimal for diurnal warming (low wind speeds near or at the center of the domain) and contain various synoptic scale shortwave events (fronts, low pressure systems) that travel generally northeastward in the northern part of the domain or westward in the southern part of the domain. The meteorological boundary condition data are taken from the NCEP Final (FNL) Operational Model Global Tropospheric Analyses product (on 1° by 1° grid, 6 hourly). This product is the result of the Global Data Assimilation System (GDAS) that collects a variety of observational data and is prepared by the GFS model system (and available on the CISL Research Data Archive). The data are linearly interpolated to hourly. Both the fluxes and SST are exchanged between the ocean and the atmosphere every 120 s.

The model microphysics uses the WRF Single-Moment 3 scheme [*Hong and Lim*, 2006]. The longwave radiative transfer scheme is the rapid radiative transfer model (RRTM) scheme [*Mlawer and Clough*, 1997] and the shortwave radiative flux scheme is the Dudhia scheme [*Dudhia*, 1989].

The surface layer physics are parameterized by the MM5 Monin-Obukhov scheme and cumulus parameterization is the Kain-Fritsch scheme [*Kain*, 2004]. *Song et al.* [2009] showed that the *Grenier and Bretherton* [2001] (herein referred to as GB) planetary boundary layer (PBL) scheme had overall better agreement with QuikSCAT observations, so it was also used for our simulations. We did perform tests with the Yonsei University scheme (YSU) [*Noh et al.*, 2003] and noted that in general, the GB PBL scheme produces much smaller spatial scale, large amplitude changes in many atmospheric meteorological variables as compared to the YSU PBL scheme. It is not our intent to evaluate the accuracy of each PBL scheme, but we will note that the results outlined in the paper are subject to sensitivities in the PBL scheme used.

3.2 Skin Temperature Algorithm

Version 3.5 of the WRF-ARW system includes a skin SST algorithm from *Zeng and Beljaars* [2005] (herein referenced as ZB). This is a prognostic scheme that computes the cool-skin temperature difference via the net fluxes and the warm layer temperature difference via the net flux and ocean turbulent mixing with a fixed mixed layer depth based on the one-dimensional heat equation [*Pielke*, 2013]. The time tendency of the diurnal cycle is expressed as:

$$\frac{\partial}{\partial t}(T_{-\delta} - T_{-d}) = \frac{Q + R_s - R(-d)}{d\rho_w c_w \nu/(\nu+1)} - \frac{0.5(\nu+1)}{\tau_e}(T_{-\delta} - T_{-d}) \tag{3.1}$$

where t is time, T is the sea water temperature, δ is the thickness of the sublayer (for the cool-skin), d is the depth at which the diurnal cycle can be omitted, Q is the surface fluxes (longwave + sensible heat flux + latent heat flux), R is the net solar radiation flux, R_s is the net solar radiation flux at the surface, ρ_w and c_w are the density and heat capacities, respectively, of sea water, ν is an empirical parameter based on *Fairall et al.* [1996b], and τ_e is the e-folding time scale of the relaxation of the warm layer ($T_{-\delta} - T_{-d}$). *Bellenger and Duvel* [2009] and *Filipiak et al.* [2012] have determined that this particular algorithm overestimates warming under 1.5K and underestimates warming over 1.5K, which can be attributed to the fixation of the mixed layer depth at 3 m. This means that the integrated heat is fixed per unit volume. If the depth of the warm layer is in actuality smaller than 3 m, as is the case when diurnal warming is large, then the diurnal warming in the model is smaller because the net heat is integrated over a larger volume than necessary. In terms of the experiment, this means that the diurnal sea surface gradient produced will be,

in general, more board in space and smaller in amplitude. As we will show in Chapter 4.2 that while there is modest accuracy of the diurnal warming model, the distribution of the amplitudes of diurnal warming are similar to those observed.

3.3 SST Boundary/Initial Conditions

The daily simulations use a foundation SST that is akin to a nighttime, convectively well-mixed temperature. The Multiscale Ultrahigh Resolution (MUR) SST product from NASA's Physical Oceanography Distributed Active Archive Data Center (PO.DAAC) is a Level 4 Foundation SST blended from skin and subskin SST nighttime observations from instruments including the Advanced Microwave Scanning Radiometer-EOS (AMSRE), the Moderate-Resolution Imaging Spectroradiometer (MODIS), WindSat microwave radiometer, and in situ SST observations. The data are remapped from 1 km grid to the nearest 25 km domain grid point by averaging the data with the nearest 25 km radius. The diurnally varying run also used the MUR data as its initial boundary condition until the development of heating occurs on the first day, at which time the SST skin algorithm calculates a new skin temperature that is sent to the surface flux physics packages in WRF.

CHAPTER 4

TWO-WAY COUPLED SIMULATION COMPARISONS

4.1 Synoptic Conditions

For this research, we focus on two case studies during 7-14 July, 2014 and 1-8 August, 2012. Each of these time periods was chosen on the basis of the presence of predominantly clear skies and low wind speeds (below 10 m/s) for a large region of the domain while having distinctly different synoptic variability (Figure 4.1 and Figure 4.2). It is important to look at the impact of diurnal variations in sea surface temperature on multi-day scales to understand continual amplifications of nonlinear reactions of the atmosphere. In the July simulation, several small storm systems cross into the domain from the south and track to the west while several larger frontal systems track east from the north. The August time period is a bit more quiescent and especially productive for diurnal warming because a dominant, semi-stationary high pressure system is seated above the central portion of the domain and very low wind speeds are frequent in this area.

4.2 Modeled Diurnal Warming and Near-surface Variability

Each simulation begins at 0Z (nighttime for this region) and the sea surface temperatures begin to heat during the course of the day, beginning roughly at 9Z. Therefore, there is no specific removal of spin-up time because neither model differs from each other until the diurnal heating begins to occur. Figure 4.3 shows a time series example of the development of diurnal warming, wind speed evolution, and incident solar radiation at the location 34°N, 51°W. The temporal evolution (shape) of diurnal warming is quite consistent with observations and other models as it takes on a bell-curve resemblance, reaching a maximum near 19Z (roughly 7 PM local time). As the heating of the day decreases from sunset onward, the diurnal heating slowly decreases as the warmth is either mechanically mixed or eroded through the bottom of the warm layer. It reaches a nighttime minimum just prior to sunrise on the next day. The ZB algorithm contains a cool-skin correction to the skin temperature. The time series of diurnal warming (which is calculated as the difference

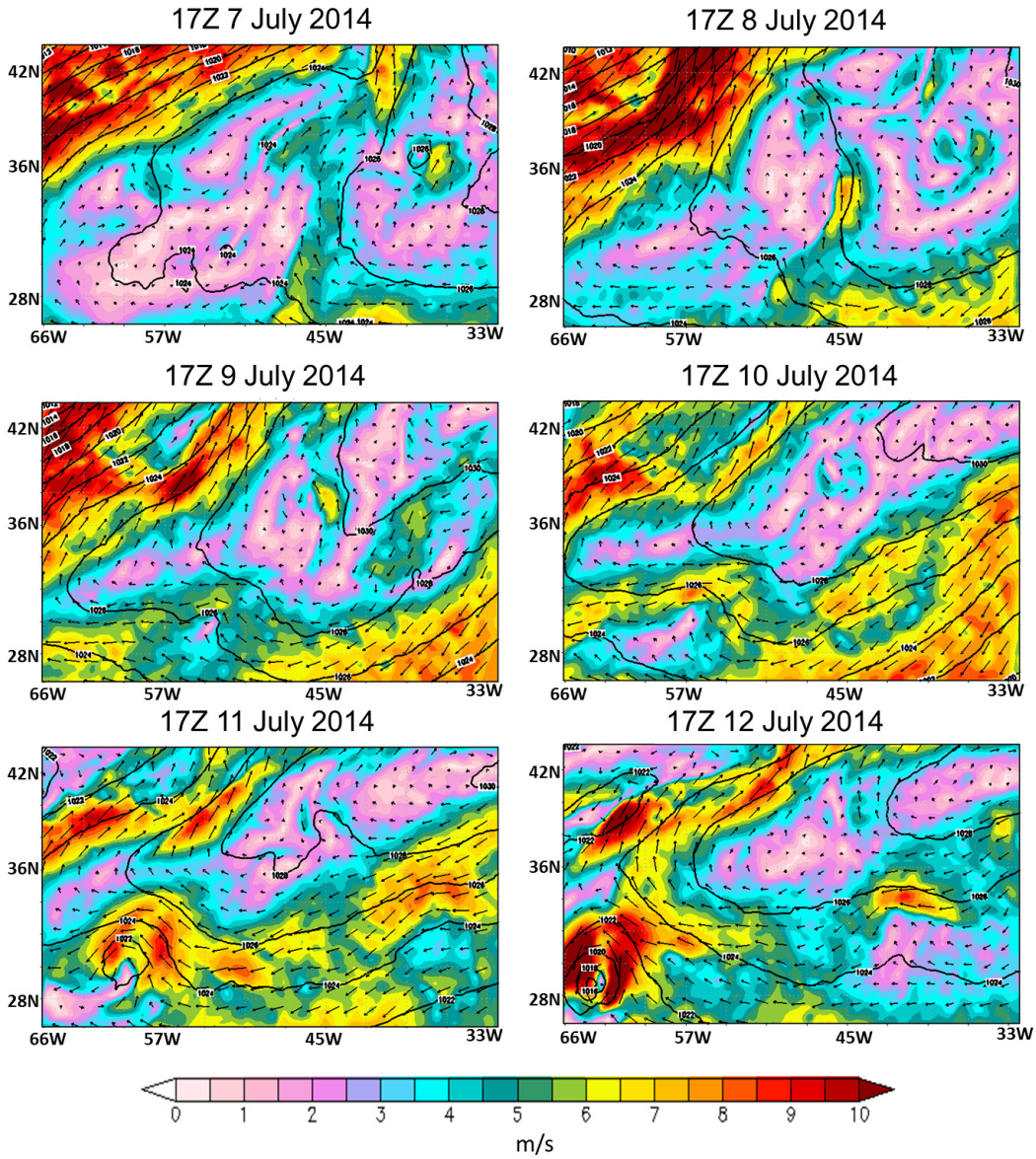

Figure 4.1: Wind speed (m/s, colored vectors), surface pressure, (mb, dashed contours), and magnitude of diurnal warming of SST (K, gray, solid contours) each day at 17Z for the week of 7-14 July, 2014.

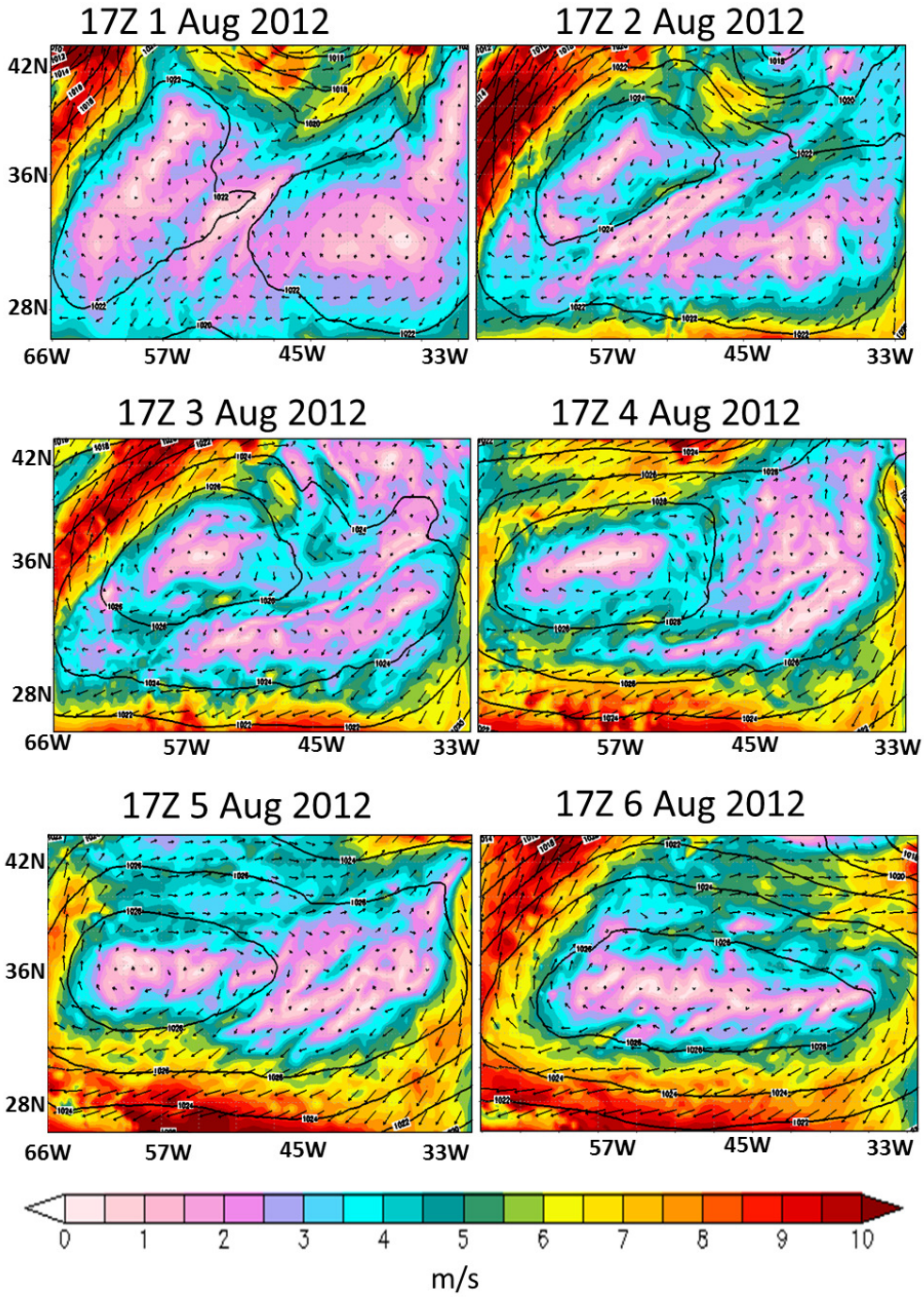

Figure 4.2: Same as 4.1 for 17Z, 1-8 August, 2012

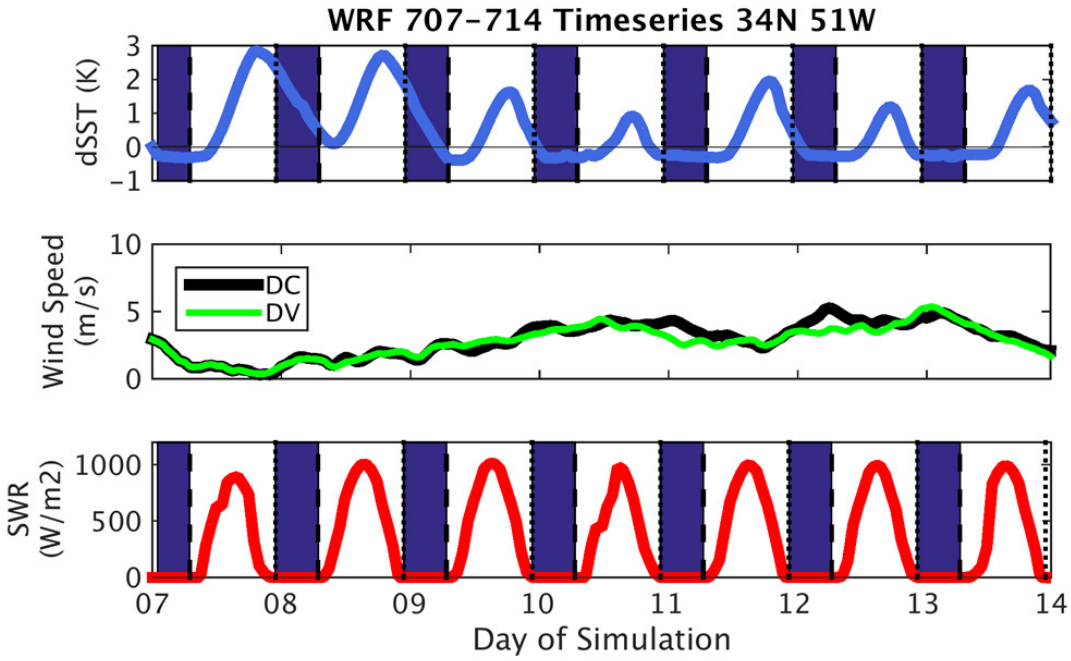

Figure 4.3: Time series of (top) magnitude of diurnal warming (K, light blue), wind speeds (m/s) for the diurnal (green) and daily-constant run (black), and incident surface solar radiative flux (W/m^2, red) at the grid point located 34°N, 51°W. Dark shaded areas represent nighttime hours for this particular location.

between the skin temperatures of the two simulations) can become negative due to the presence of the cool-skin bias that is not evident in the MUR data. More details are provided in Chapter 5.

Figure 4.4 shows the extent of warming that develops over the course of the day on 7 July, 2014. At the time of maximum diurnal warming, roughly 50% of the domain experiences warmer ocean surface temperatures >0.5 K. The maximum amplitude of diurnal warming of SSTs found is 3.94 K for the July simulation and 6.59 K for the August simulation. *Merchant et al.* [2008] found satellite-based values of diurnal warming that commonly exceed 4 K using SEVIRI SST data within the Mediterranean Sea and noted a few cases that exceed 6 K. They do remark, however, that the spatial scales of these extreme events are on the order of the analysis scale itself and warrant further investigation. *Gentemann et al.* [2008] also found similar peak diurnal warming magnitudes of roughly 6.4 K, 4.4 K, and 4.2 K in MODIS, SEVIRI, and AMSR-E datasets respectively in various locations in the Atlantic Ocean. Figure 4.5 shows the probability distribution of the diurnal

warming for both July and August simulations; similar shape of the distributions can be found in *Merchant et al.* [2008].

Figure 4.6 shows the weekly composites of diurnal heating, as well as differences in 1000 mb air temperature, sea level pressure, latent heat flux, and wind speed. In July, the average peak in diurnal warming is roughly 1 K while the average peak in the August simulation exceeds 1.5 K. As expected, the region above the location of diurnal heating coincides well with an albeit small mean surface pressure decrease and increase in the lowest model level air temperature (not shown). Surface pressure decreases are on the order of 0.4 hPa and comparable in magnitude to other SST-induced pressure perturbations along mesoscale meanders in boundary currents [e.g. *O'Neill et al.*, 2010]. The lowered pressure and location of diurnal warming is also well correlated with the increase in latent heat flux (roughly 10-15 W/m^2 on average) and sensible heat flux (not shown) from the diurnal warming. Hourly variations of the latent heat fluxes in localized areas increased by more than 50 W/m^2. These measures provide confidence that the atmospheric feedbacks imposed by the diurnal warming are evident in the WRF near-surface boundary layer processes and the nature of the diurnal warming is consistent with previous studies.

The mean fields, however, do not necessarily depict the highly dynamic nature of the boundary layer changes on an hourly basis. While the mean pressure differences locally over the diurnal warming are typically <1 hPa, we also observe several instances of larger amplitude (1-2 hPa) pressure anomalies. More specifically, these are areas that contain both positive and negative pressure and wind differences within close proximity and coincide with storm systems in each simulation. Figure 4.7 shows the mean pressure differences at a period late into the simulation (23Z July 11 - 10Z July 12) and the approximate minimum pressure locations of a storm system tracking to the southwest in each simulation over the course of 40 hours. There is roughly a 100 km difference in the initial storm position in the diurnal warming simulation as compared to the daily-constant simulation. Eventually as the storm becomes a bit stronger, the tracks converge, but the residing pressure minimums differ by a few millibars. It is not clear in what physical manner diurnal warming plays in changing the dynamics of the atmosphere of the storm system; rather we can only observe that diurnal warming was not developing locally under the storm systems (storms have too high of winds) and thus the displaced storm systems were affected by the earlier regional diurnal warming and the atmosphere's transport of its energy.

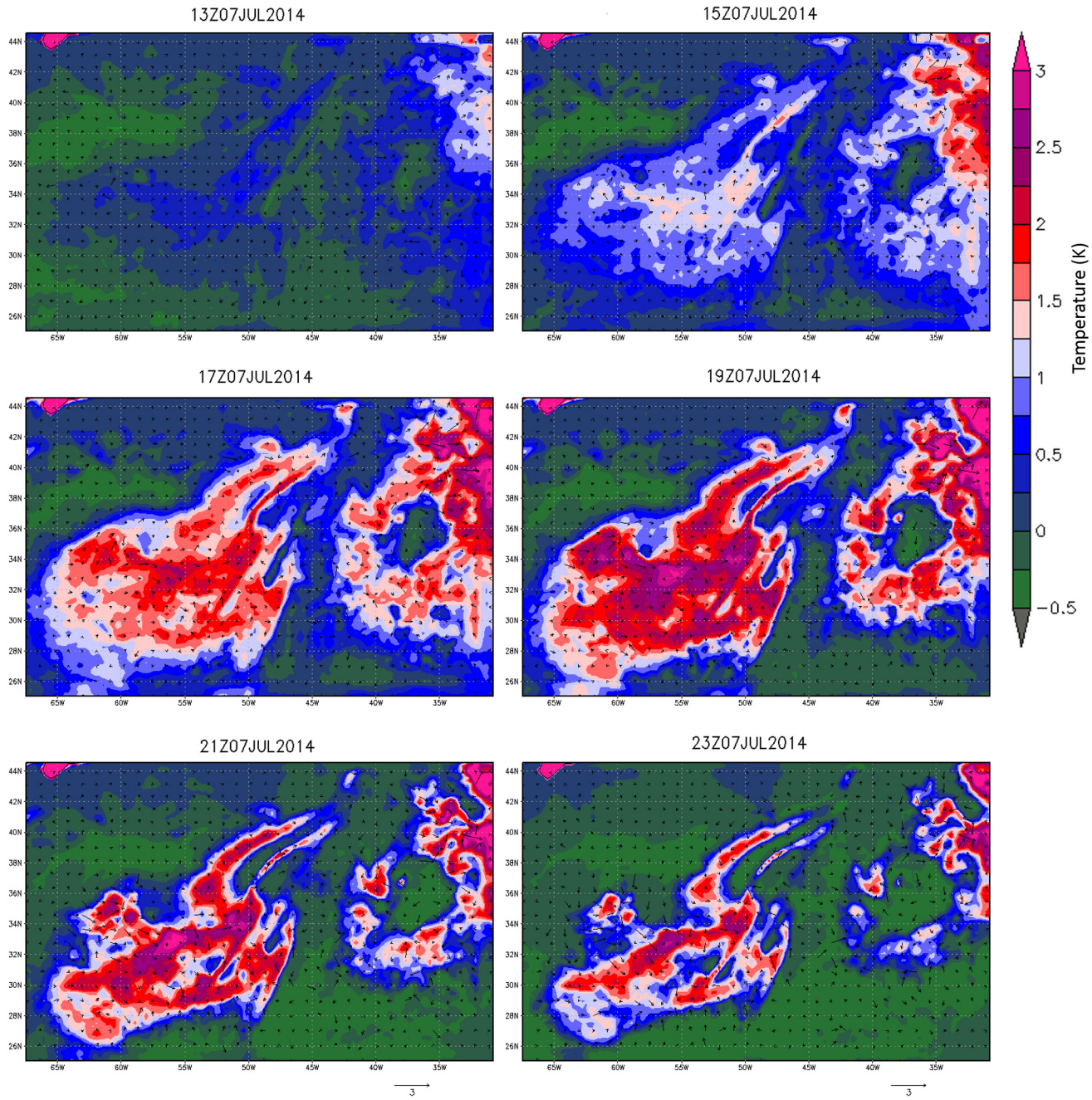

Figure 4.4: Magnitude of diurnal warming (K) (shaded) and the wind difference vector between the diurnal warming minus the daily constant run for 7 July at 13Z (top left), 15Z (top center), 17Z (top right), 19Z (bottom left), 21Z (bottom center), and 23Z (bottom right).

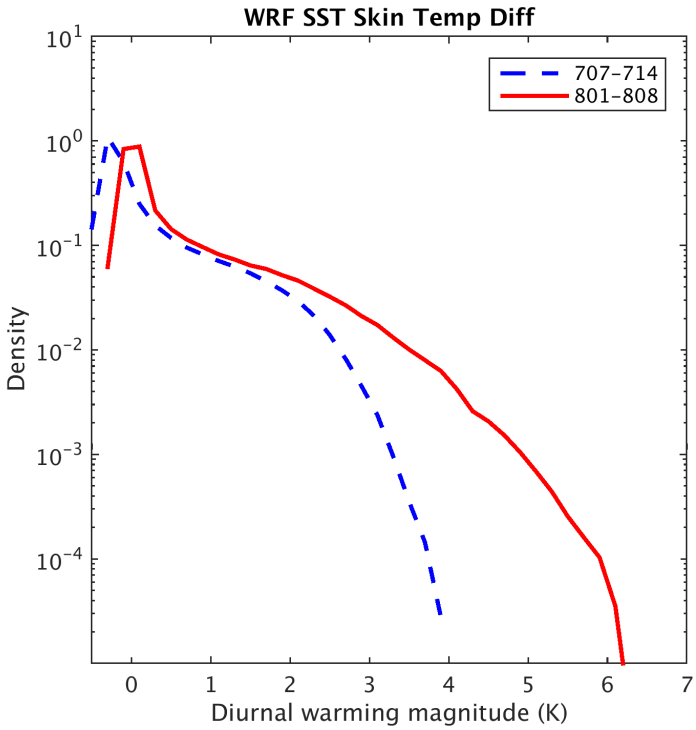

Figure 4.5: Probability density function of the magnitudes of diurnal warming for the July simulation (blue dashed line) and the August simulation (red solid line).

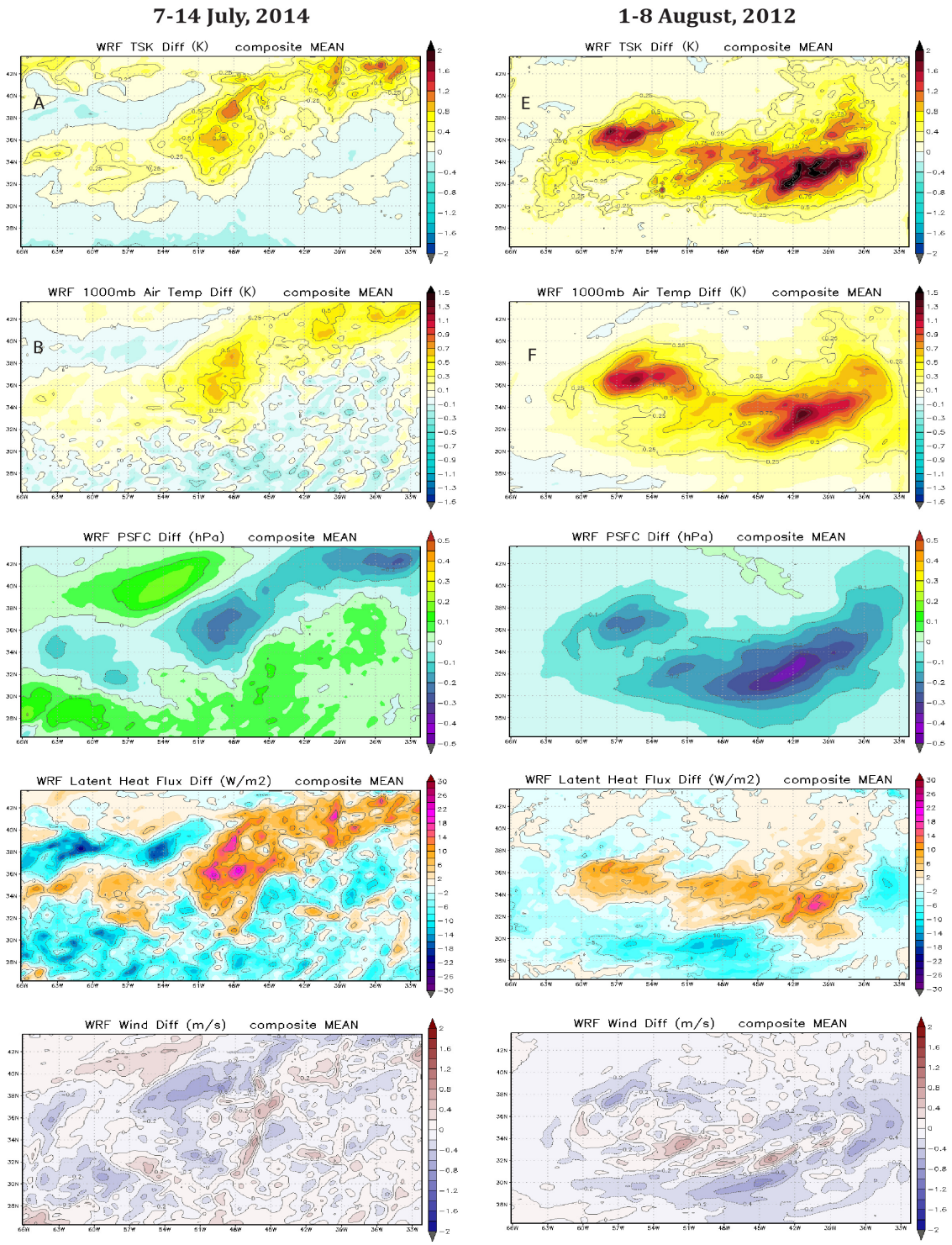

Figure 4.6: Mean differences in (top row) diurnal warming (K), (second row) air temperature at 1000 mb (K), (third row) pressure (mb), and (bottom row) wind speed (m/s) of the 7-day simulation for 7-14 July, 2014 (left column) and 1-8 August, 2012 (right column). The mean magnitude of diurnal warming (K) is plotted on the wind speed differences for reference.

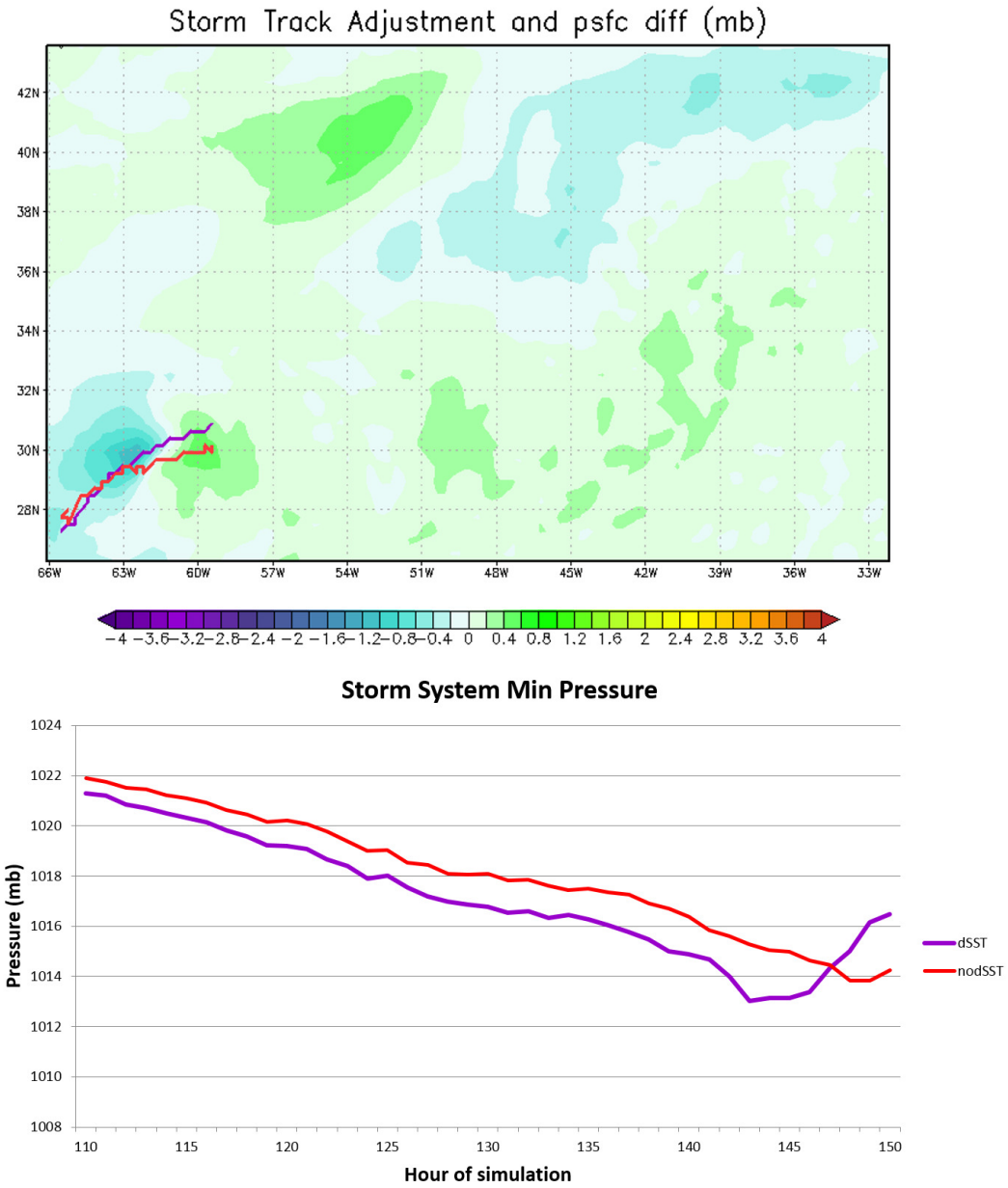

Figure 4.7: Mean sea level pressure differences (top) and approximate minimum pressure locations (bottom) for a storm between dSST simulation (purple) and the daily-constant simulation (red). The pressure differences are averaged over 23Z 11 July and 10Z 12 July and the position of the storms are from 13Z 11 July to 5Z 13 July.

Figure 4.8 shows the height extent of +1 K heat anomaly surface in the atmosphere as a result of diurnal warming. Note that these are not strictly trajectories of heat anomalies, but the surfaces represent a change in the temperature at a given model level. The extent of temperature changes (likely from the surface) is restricted to the boundary layer roughly within the first day. But, as time progresses, the anomalies occur much higher in the atmosphere via various atmospheric interactions. It is surprising to see that the changes to the temperature in the July simulation are located well into the free atmosphere even though the atmosphere coinciding with locations of diurnal warming are typically statically stable (under high pressure). In comparison, the heat extent in the August simulation, wherein a stronger high pressure system is centered over the domain, is much more limited to the boundary layer. Thus, it appears that, under certain conditions, the presence of diurnal warming modifies the local surface winds, temperature, and pressure, beginning at the surface, and the evolution of these fields is such that the regional weather is also substantially modified. Figure 4.9 shows the amplitude of diurnal warming, and the differences in wind speed, upward velocity, and outgoing longwave radiation at 19Z on 8 July, 2014. One particular point of interest is 48°W, 32°N where the diurnal warming gradient is large, followed by an increase in wind speed, vertical velocity, and outgoing longwave radiation with the inclusion of diurnal warming. This feature, again, demonstrates that the diurnal warming has the ability to affect not only the marine boundary layer but the convection occurring within the free troposphere. This particular area will be further investigated in section 6.2 using a momentum budget analysis. *Minobe et al.* [2008] studied the impact of the Gulf Stream SST gradients on the troposphere using satellite and modeling observations and determined that the long-term surface pressure adjustments and wind convergence could be responsible for the narrow band of precipitation positioned atop the SST gradient. They deduced that SST gradients can, in fact, impact the entire troposphere, both locally and regionally. *Hashizume et al.* [2001] detected rainfall anomalies in the southern portion of the intertropical convergence zone (ITCZ) in association with tropical instability waves of SST, also suggesting that the atmospheric response is not limited to the PBL depth over the warmer waters. If the same or similar mechanisms are at play, it suggests that the ability of diurnal SST to impact the model's free troposphere could be realistic.

Finally, the composites of the changes to the wind field appear far less correlated with the locations of diurnal warming, but on average, are as large as 0.4-0.6 m/s for both positive and

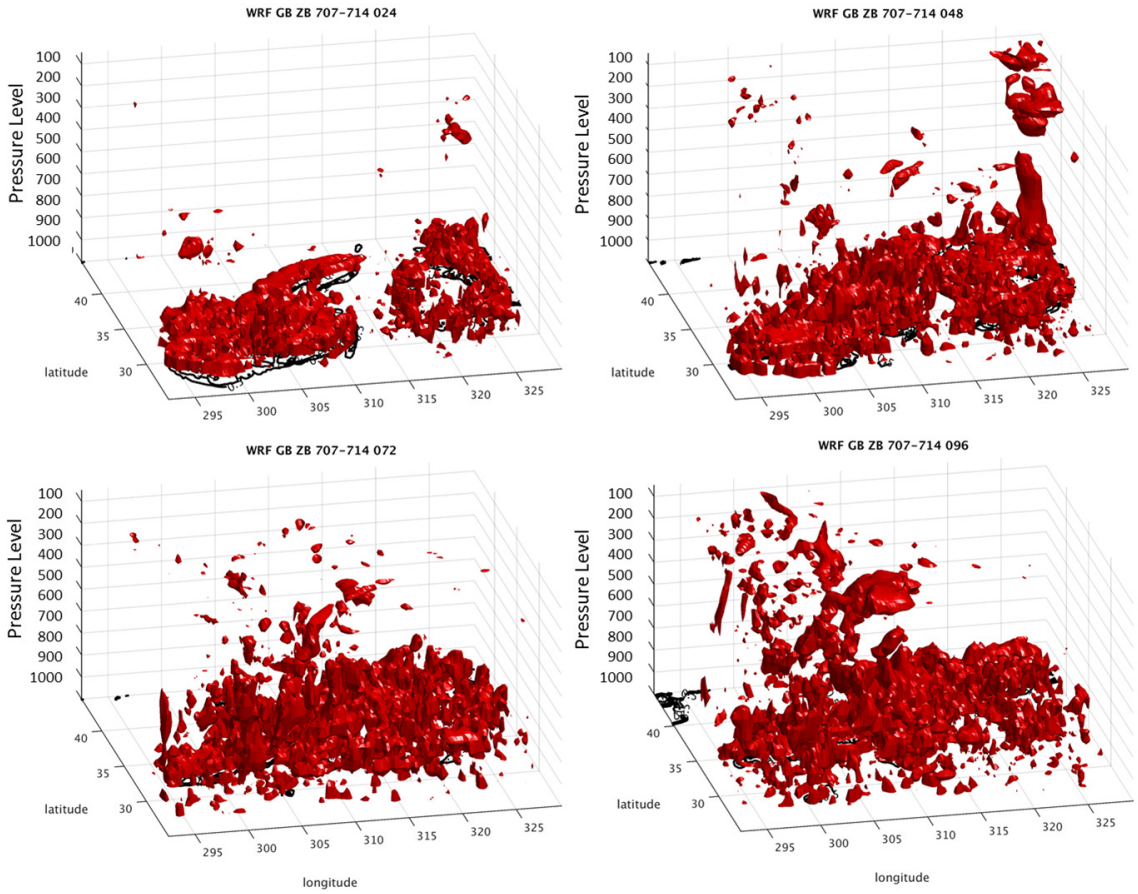

Figure 4.8: 3-dimensional surface of the +1K atmospheric temperature anomaly at 23Z (24th hour of simulation) on (top left) 7 July, (top right) 8 July, (bottom left) 9 July, and 10 July. The diurnal warming magnitude (K) is contoured in black.

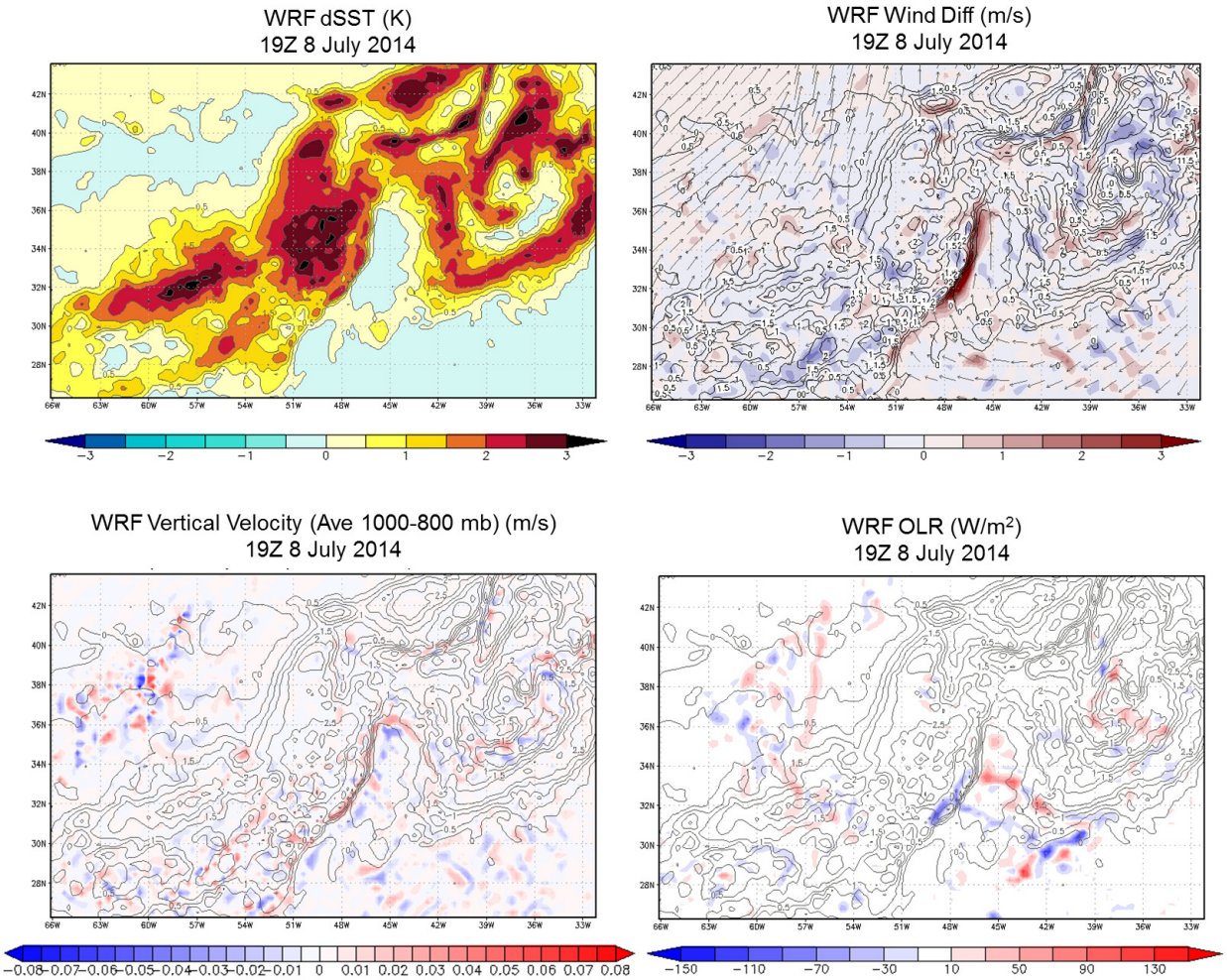

Figure 4.9: Diurnal warming magnitude (K, top left), difference in wind speed (m/s, top right) wind vectors from the diurnally varying simulation, averaged upward velocity between 1000 mb to 800 mb (m/s, bottom left) and outgoing longwave radiation (W/m^2, bottom right) at 19Z 8 July, 2014. The magnitude of diurnal warming (K) is contoured.

negative anomalies and comparable to references herein. As mentioned previously, many large wind anomalies exist due to the shift in storm tracks. However, this does not explain all the variability in the wind speed changes. Chapter 6 will investigate the presence of wind anomalies away from storm systems and examine their role with respect to SST diurnal variability.

CHAPTER 5

EVALUATION OF SST AND WIND CHANGES

As previously reported, the ZB algorithm is expected to have modest skill in predicting the diurnal cycle of SSTs based on previous studies [e.g. *Bellenger and Duvel*, 2009]. To verify this, we compare the best fit of the foundation SST and modeled SST to geostationary satellite data due to its high temporal sampling over the day of the same area of the globe. Furthermore, we investigate certain potential uncertainties within our comparison of the products. Comparisons were only completed for the July simulation due to geostationary data availability.

Two geostationary satellites were used in this study: the Geostationary Operational Environmental Satellite (GOES) L2P 4.5 km Western Atlantic Regional Skin SSTs from GOES-13 satellite (GDS v.2) and the Spinning Enhanced Visible and InfraRed Imager (SEVIRI) L2P 4.5 km Atlantic Regional Skin SSTs from the Meteosat Second Generation satellite (MSG2). The SEVIRI data are produced by the European Organization for the Exploitation of Meteorological Satellites (EUMETSAT), Ocean and Sea Ice Satellite Application Facility (OSI SAF) and made available through the Group for High Resolution Sea Surface Temperature (GHRSST) and NASA's PO.DAAC. The SEVIRI SSTs have a spatial extent from 73°N to 73°S and 81°W to 81°E. SEVIRI has a spatial resolution of 4.5 km with a 15 minute sampling rate; we used the data closest to the nearest integer hour. The GOES data are produced by the National Oceanic and Atmospheric Administration (NOAA) and also available on NASA's PO.DAAC. Its coverage is slightly smaller than SEVIRI, from 65°N to 50°S, and 135°W to 30°W with a resolution of 4.6 km by 4.2 km. Each datum is remapped to the WRF grid by taking the mean of the data within the nearest 25 km radius to reduce the effects of small scale variability and noise in the high resolution data.

Figure 5.1 shows the comparisons of the SEVIRI and GOES skin SST compared to the MUR foundation temperature (right, top row) and the modeled skin SSTs from the WRF and ZB algorithm (right, bottom row). The MUR foundation data were expected to show a cold bias compared to the geostationary data since the MUR SSTs do not contain any diurnal variability. However, the MUR data are actually warmer on average; as mentioned previously, the ZB algorithm includes

estimations of the cool-skin layer that is between 0.1 to 0.3 K. The MUR foundation temperature does not account for the cool-skin variability for this particular region. Figure 5.1 shows just one example of how the MUR foundation temperature is consistently higher at nighttime than the modeled SST and that GOES and ZB SSTs are in better agreement than GOES and MUR SST (Figure 5.2). This nighttime bias is, on average, 0.17 K. Identifying this cool-skin correction is important for a number of reasons; we need to remove this difference from the foundation temperature during the daytime because the cool-skin is always present and produces a systematic bias in comparisons to satellite data [*Gentemann and Minnett*, 2008]. Those who desire to properly model the entire diurnal cycle of SSTs (even at night) or to verify nighttime-based algorithms of future satellite missions will require an estimation of the cool-skin effect. The cool-skin is an important factor in the mean heat budget of the upper-ocean and can influence the rate of convective overturning [*Fairall et al.*, 1996a; *Wick et al.*, 2005].

GOES initially has a higher mean bias from MUR as compared to SEVIRI, but when bias corrected as well as using its full sample of data, the mean bias is reduced from -0.43 K to -0.195 K. We will focus on the comparison to GOES data because GOES also has 3 times more data coverage during this time period and region than SEVIRI and therefore contains a more complete coverage of the diurnal cycles. During the day time, the comparison to the entire GOES record shows that WRF modeled SSTs are overestimated by 0.5 K on average even when bias corrected for the cool-skin effect. We do not expect the differences between the SSTs to be an artifact of daytime undersampling because GOES has slightly higher SST retrievals during the afternoon hours as compared to nighttime (Figure 5.3). In fact, the most temporal undersampling is during the hours closest to sunset and sunrise; this is likely the result of the data quality flagging from the retrieval algorithm when switching from nighttime and daytime algorithms [*Maturi et al.*, 2008]. We also verified that the overestimation was not the result of a low wind speed bias in the WRF data. The wind speeds are verified against Advanced Scatterometer (ASCAT) 12.5 km winds from the MetOP-A satellite. Note that the 12.5 km product is used because the effective resolution matched our 25 km grid. As compared to ASCAT data, the wind speeds in WRF are actually biased high under conditions of diurnal warming (for 1K magnitude of diurnal warming, WRF wind speeds are 0.5-2 m/s (25th,75th percentile) larger). This is actually quite consistent with *Bellenger and Duvel*

[2009] and *Filipiak et al.* [2012], who found that the ZB algorithm overestimates diurnal warming under moderate winds (winds =5 m/s) and underestimates diurnal warming under light winds.

We also must consider that part of the error seen in the comparison can arise from factors other than the ZB algorithm. One source of potential error is the result of smoothing the geostationary data to the 25 km model resolution. GOES reproduces a fairly muted diurnal cycle in the SSTs of 0.5 K on average, whereas the average diurnal cycle in the WRF simulations is about 1 K (not shown). We have averaged the geostationary data to within the nearest 25 km grid point in order to reduce the effect of high ratio noise in high resolution products. The consequence is that we have potentially smoothed out small spatial variability in the satellite data [*Filipiak et al.*, 2012] in which large amplitude diurnal warming >2 K are known to occur on spatial scales of 60 km [*Merchant et al.*, 2008; *Clayson and Bogdanoff*, 2013]. *Noh et al.* [2011] hypothesized that a portion of their relatively large root mean square error (0.72 K) in their point-by-point matches of the amplitude of diurnal warming to satellite data could be the result of differences in the atmospheric forcing and real world conditions. This also includes pixel-by-pixel error from the small spatial scale SST variability around western boundary current edges and/or subpixel SST mesoscale fronts. Therefore, the error relating to the ZB algorithm could be overestimated.

It is unreasonable to assume that an empirical algorithm will be able to reproduce diurnal warming in every given situation. Nonetheless, we are encouraged that the ZB algorithm produces a distribution of diurnal warming amplitudes within reason. According to *Filipiak et al.* [2012], in this respect, models that can reproduce the full distribution of diurnal variability are considered viable for calculating the overall "mean effect of diurnal variability on processes that are non-linear in SST, since the full distribution of diurnal variability determines the mean effect". Furthermore, as we will show in Chapter 7, studies that use the ZB algorithm with external forcing data to diagnose the effect on fluxes, for example, can be additionally overestimating the warming if fluxes, winds, and SST are not fully coupled.

We will close this section by elaborating more on the accuracy of the modeled wind fields compared to the swath ASCAT-A data. Figure 5.4 shows that the collocated winds and WRF modeled data over the course of the July simulation. Rather than focus on the best fit statistics, which are probably not statistically different between the simulations based on the number of independent observations, we will remark on the reduced scatter of the extrema. One distinct difference in the

comparison of diurnally varying versus the daily-constant simulation is the reduction of large wind speeds produced by the WRF model simulation around 10 to 14 m/s. Some of these outlying wind speeds are significantly reduced (by 2 to 4 m/s). These large wind speeds are likely generated from storm systems within the region. We have identified significant positive and negative changes to the wind, pressure, and temperature that occur in very close proximity to one another in these storms systems. Because the large changes are fairly symmetric, they are better interpreted as changes to the storm track rather than modifications of the amplitude of the storm. The comparisons of the satellite winds could be showing that the representation of the storm tracks is more realistic when diurnal variability of SSTs is considered.

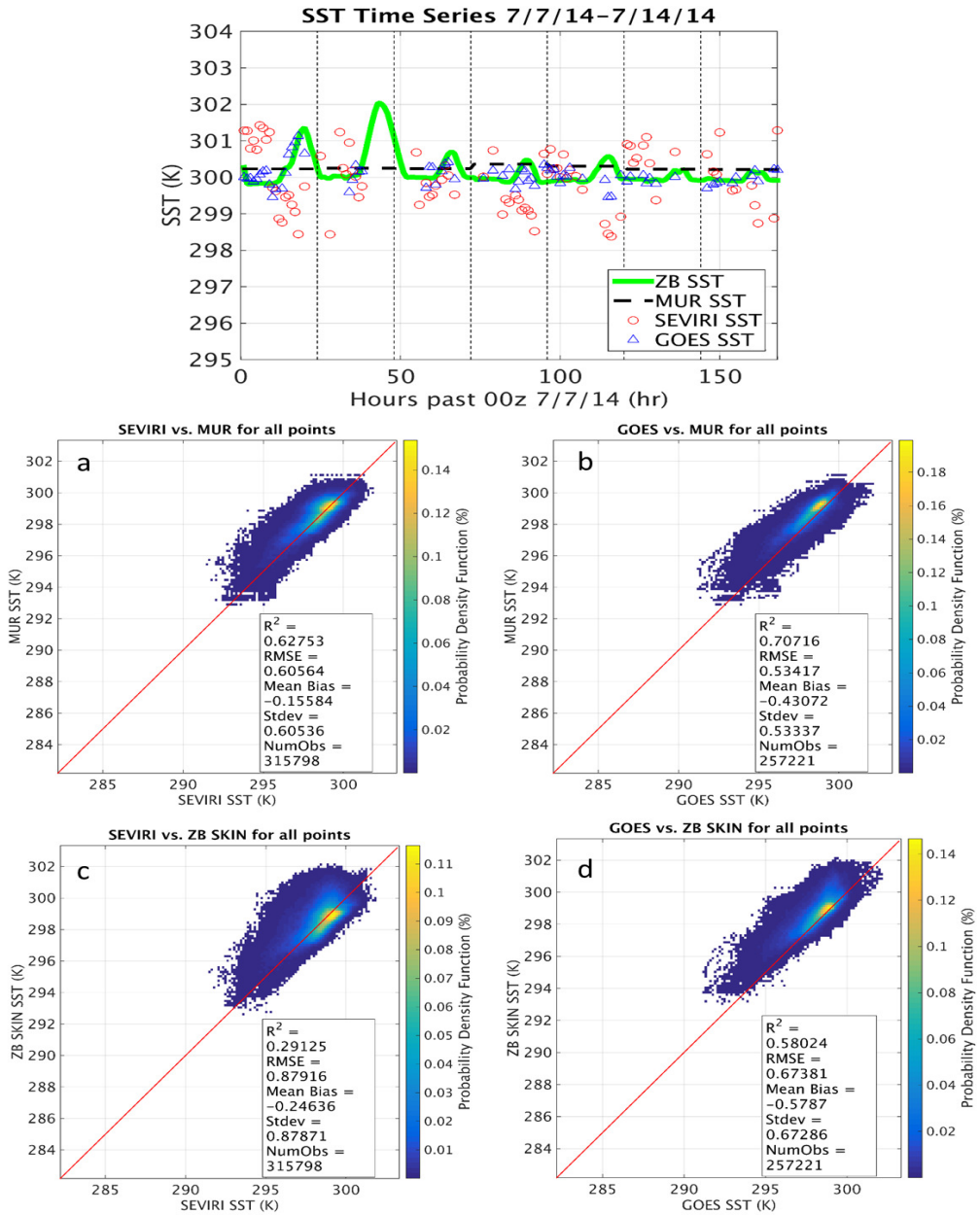

Figure 5.1: (Top) Time series of modeled skin SST (K) from the ZB algorithm (solid green), MUR foundation SST (dashed black), SEVIRI skin SSTs (red circles), and GOES skin SST (blue triangles). (Four panels) Comparisons of a) MUR foundation vs SEVIRI skin SST, b) MUR foundation vs GOES skin SST, c) ZB modeled skin vs SEVIRI skin SSTs, and d) ZB modeled skin vs GOES skin SSTs. For figures b and d, only GOES data points where SEVIRI data exist are used. The mean bias is calculated by subtracting the y-axis SST from the geostationary data.

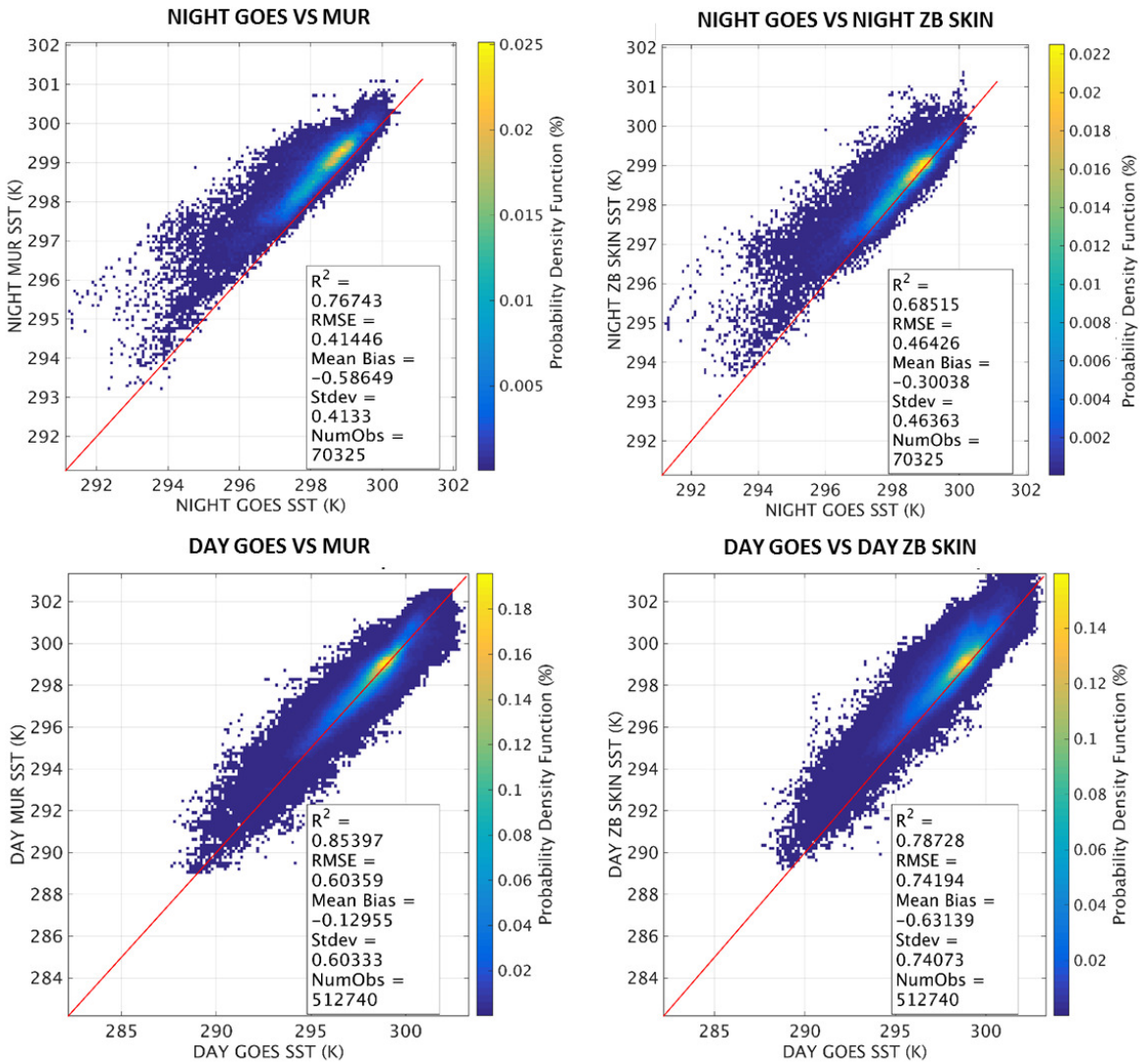

Figure 5.2: Comparisons of (top left) MUR foundation SSTs vs nighttime only GOES skin (K), and (top right) nighttime only data from ZB modeled SSTs vs nighttime only GOES skin SST (K), (bottom left) MUR foundation SSTs vs daytime only GOES skin SST (K), and (bottom right) daytime only ZB modeled SSTs vs daytime only GOES skin SST (K).

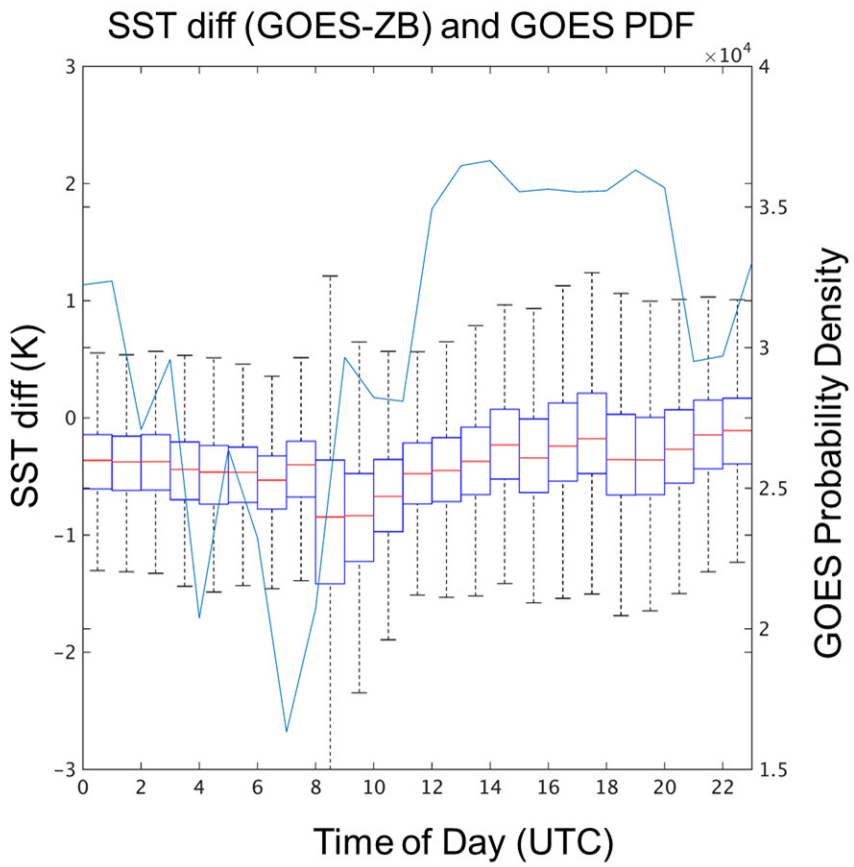

Figure 5.3: Boxplot distribution of the differences in SST (GOES-WRF) (K) (left axis) and the probability density of GOES SST sampling (light blue solid line) (right axis) as a function of Greenwich Mean Time. The boxes represent the 25th and 75th quartiles and the whiskers represent a 95% confidence level.

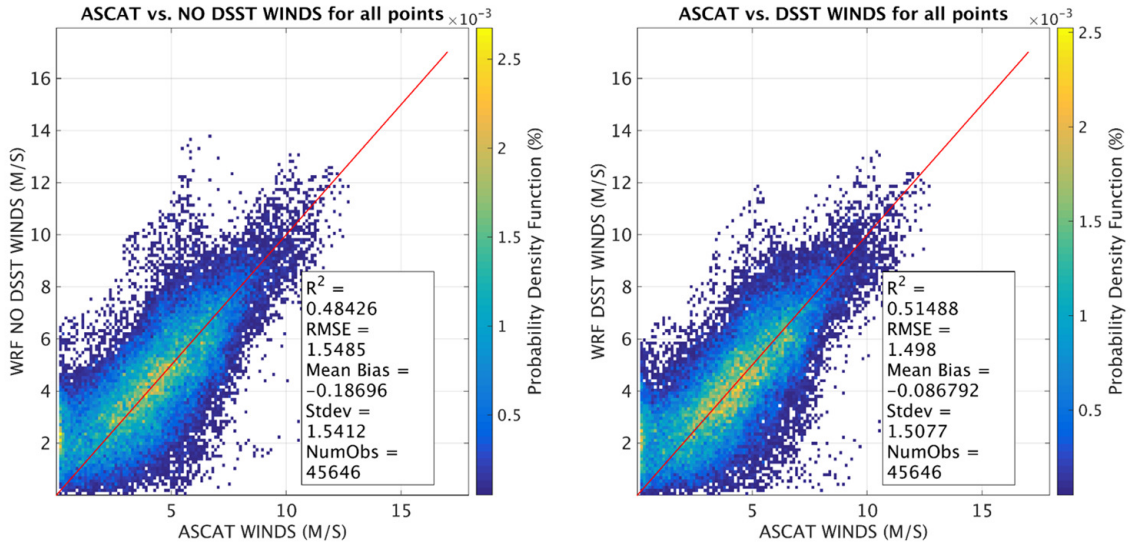

Figure 5.4: Comparisons of (left) wind speeds from the daily-constant simulation vs ASCAT-A (m/s) and (right) modeled wind speeds from the diurnally varying simulation vs ASCAT-A for the July simulation. Shaded values indicate the data density of the scattered data.

CHAPTER 6

NEAR-SURFACE WIND FIELD RESPONSES

Recent satellite and modeling studies have discussed role of SST and wind coupling in terms of the anomalous wind response surrounding strong and weak SST gradients and the effect on the marine boundary layer [e.g. *Sweet et al.*, 1981; *Lee-Thorp et al.*, 1999; *Chelton et al.*, 2001, 2004; *Park and Cornillon*, 2002; *Song et al.*, 2006, 2009; *O'Neill et al.*, 2010; *O'Neill*, 2012]. Most of these studies analyzed SST perturbations associated with western boundary currents, tropical instability waves, or eddies and performed some kind of spatial filtering and/or temporal averaging in their analysis. For example, *Chelton et al.* [2001] showed three-day averages of QuikSCAT wind stress divergence and curl along with SSTs in the equatorial Pacific cold tongue (where Coriolis is negligible) and determined that the changes of wind stress divergence and curl were well correlated with the direction of flow over the SST isotherms. These analyses were filtered to remove variability with wavelengths longer than 4° in the zonal direction to avoid sampling errors or large weather variability. It is not clear from these studies on what time scales the wind-SST anomaly coupling occurs.

However, *Bourras et al.* [2004] used an analysis of wind anomalies from SSM/I and QuikSCAT and observed a weakening response to a cool mesoscale SST anomaly every 1 to 10 days over the course of 3 months. This anomaly was studied as part of a larger mesoscale cyclonic circulation in the northeast Atlantic during the POMME experiment in 2000-2001. *Lambaerts et al.* [2013] studied an idealized WRF scenario wherein weak easterly winds travel over SST anomalies in the spatial form analogous to SST height anomalies. They showed that the atmospheric dynamical response (changes in the upward wind component) occurred just within a few hours and occurred on mesoscales and submesoscales. These studies provide confidence that we could expect wind-SST anomaly coupling to occur on daily or subdiurnal timescales within our simulations.

In our study, we aim to compare the evolution of wind speeds in response to a diurnally produced SST gradient. Our context differs from the studies listed above because the variations in SST studied herein are almost completely the result of atmospheric forcing rather than ocean dynamics.

6.1 Composite Wind Changes

On an hourly basis, the changes to the wind field are quite variable in space. Both small scale features (wavelengths > 100 km) and larger scale (>400 km) are frequent, propagate through space and time, and can have amplitudes of >3 m/s at times (especially within the storm systems). More often, they have a range of 0.5—2 m/s that is quite consistent with previous SST-wind studies referenced herein. In order to determine whether a spatial relationship exists with the wind changes relative to the diurnal warming, we computed the composites of the wind speed difference (Figure 4.6) as well as the mean wind divergence and wind stress curl for both time periods (Figure 6.1). If we expect the wind fields to respond similarly to that of *Chelton et al.* [2001] [and other references herein], we anticipate a mean increase in the wind vector along the maximum diurnal warming gradient (flow from cold to warm) when winds are perpendicular to isotherms of the diurnal warming.

For flow parallel to isotherms of the diurnal warming, we would expect a mean increase to the wind stress divergence over the maximum diurnal warming gradient with warmer water to the right of motion. However, the seven-day mean fields of surface divergence and wind stress curl do not reveal this pattern. The interpretation of the July simulation (left hand column) is particularly vague because the composite differences in surface divergence have large spatial variability and are small in amplitude. Alternatively, for the August simulation, the diurnal warming and surface divergence are better correlated, but lacking in a specific spatial pattern in reference to the mean wind direction and speed. We believe that the wind stress curl differences only highlight the fact that the smallest wind vectors have the most directional variability, rather than a particular influence by the diurnal warming of the sea surface. This was also confirmed by performing an empirical orthogonal function (EOF) to determine the dominant modes of variability. The first EOF only described 10% of the variability and also did not appear to show dependence on the mean flow across the diurnal warming.

Rather than focusing on the mean wind speed changes, we also investigated the distributions of the wind speed field derivatives relative to direction of the flow across the diurnal warming gradient. We projected each wind vector onto the along-flow and cross-flow components of the diurnal warming gradient vector. The along-flow component gives a measure of the wind speed flowing toward or away from the diurnal warming (divergence) and the cross-flow components

describe the vorticity of the wind vector (curl). We would expect that when the cross-gradient component is approximately zero, the wind vectors in the along gradient direction should increase (consistent with an increase in curl) as they flow with warm water to the right of motion. Conversely, when the along-gradient is approximately zero, we would expect to see the most substantial increases to the cross-gradient vectors if the established SST-wind coupling mechanism holds. Figure 6.2 shows the probability distributions of the cross and along-flow gradient vector wind components as a function of the wind speed difference in the model for the August simulation. Each line in the probability distribution plotted on the left represents the data where the along-track (w_a) is greater than, less than, and nearly zero. To approximate "nearly zero", a window is chosen that is equal to 1/2 the standard deviations of the along and cross vector components based on their individual distributions. From these results, there is not a consistent shift in the distribution with the cross-gradient component relative to the flow of the wind over the diurnal warming gradient that would indicate a clear increase or decrease in the divergence fields. There is a slight shift in the along-vector component towards increasing wind speeds at the right tail of the distribution, but this change is likely the result of the Coriolis deflection.

Another method for determining the potential relationship of wind and diurnal SST coupling is to look at the distributions relative to time. In analyzing the wind speed changes relative to time of day, there is an apparent lag between the maximum heating of the ocean surface and the wind response. Figure 6.3 shows the distributions of the wind speed differences (at time t+lag) as a function of the directional derivative of the dSST gradient occurring at t=17 hours into the simulation (positive represents the winds flowing from cold to warm SST). This methodology would work if we assume the advection of anomalies is negligible. To a first order, this assumption is considered adequate because the atmosphere is relatively statically stable over the areas of, but prior to, diurnal warming. At t=17, most of the region in the simulation is well into its local afternoon and diurnal warming of the ocean has developed. We wish to examine what happens to the local winds as a function of 1 through 6 hours prior and after diurnal warming. As time progresses onward, we see an increasing (decreasing) wind speed trend when air is flowing toward (away from) diurnally warmed SST. The green line in each box plot represents the slope of the line fitted to the median values of each bin of dSST directional derivative. This gives us a measure of the strength of the wind-SST coupling linear trend observed in *Chelton et al.* [2001] as a function

of time before and after diurnal warming has developed. We repeated this same process for each day of the simulation wherein the directional derivatives of the diurnal warming were calculated at 16Z each day and the distribution of the wind changes were plotted relative to the magnitude of the directional derivative. This time, the wind changes were calculated for lag $t = 1 : 10$ hours after warming has occurred. Figure 6.4 shows the magnitude of the slope and how it varies with increasing lag time for each day. For days 1 and 2 of the July simulation, the dSST-wind coupling trend increases at each hour after diurnal warming, but the trend reverses after day 2. It is possible that the secondary feedbacks (i.e. modifications on the synoptic scale) are dominating the signal rather than the dSST-wind surface coupling.

One potential problem with the above analysis is that the potential wind effects from the diurnal warming are advected away from the diurnal warming gradient. In *Lambaerts et al.* [2013], they performed a sensitivity test on the magnitude of the background wind (by increasing the vertical shear) and found that the correlations of SST and vertical wind perturbations decrease when advection is stronger. Rather than examining the winds relative to the coincident spatial distribution of diurnal warming (or the gradient thereof), we instead can compute statistics on the variations of the time series of the individual variables. To identify any possible diurnal cycling of winds due to the variability in SST, we examined the composite wavelet spectrum of the wind speed changes for the July (not shown) and August simulation (Figure 6.5) and compared them to the wavelets of the magnitude of diurnal warming and sea level pressure change. Wavelets allow us to examine the dominant periods of variability in a time series with respect to the time of the signal. Figure 6.5 shows that for the diurnal warming and sea level pressure, an isolated maximum power exists at a period of 24 hours, thus indicating that the region, on average, experiences a healthy diurnal cycle in dSST and sea level pressure variability. The average wind differences, however, do not necessarily show an isolated power maxima at 24 hours. Instead, the power maxima is relatively constant for periods >= 24 hours. For the July simulation, there is no indication of a relative maxima in power at a period of 24 hours. Following the methodology of *Chelton et al.* [2001], we performed a low pass filter to remove variability with wavelengths less than 2, 3, and 4° of latitude and longitude on the wind speed differences and recomputed the wavelets. The low pass filter reduces the amplitude of the small scale variability generated in the simulations. Note that most of the small scale anomalies propagate consistently in space in time, likely resulting

from gravity waves generated by the shock of heat influx from the surface. In turn, the power spectra within the wavelet show an enhanced power at periods of 24 hours (Figure 6.6); thus we see a more distinct mean diurnal cycle in the winds when the small scale variability is reduced. It is believed that this periodicity is likely weighted by the periodicity found around 44°W in the August simulation (Figure 6.7). Note that the time scale increases from bottom to top and the wind vectors are world relative (east is to the right). When looking at the temporal and zonal variability at 32°N, we see that diurnal warming occurs almost the entire width of the domain, but yet, the largest wind speed differences occur within the area around 51°W - 42°W. Around 44°W, the largest increases to the wind occur over diurnal warming with large peak amplitudes (>4 K) and residual warming that is almost continuous from day to day. However, there are similar locations (e.g. 54°W) with persistent diurnal warming but relatively small changes to the wind speed.

To summarize, we have found that the diurnal warming generates near-surface hourly wind speed changes of the same magnitude as those seen with wind-SST coupling studies along tropical instability waves and ocean boundary currents. However, spatial distributions of the wind speed changes, on the whole, are not necessarily well correlated to the flow across the diurnal warming gradient; rather, we see only specific coincident dSST gradients and wind speed changes that are physically consistent with the SST perturbation/wind speed modifications on longer time scales. Rather, we have identified that, on the whole, the mean variability of wind and diurnal SSTs are not well explained as a comparison to the physical interaction of winds and SST perturbations that are driven on the longer timescales. Feedbacks to the larger synoptic scale are believed to further deter identification of diurnal coupling of winds and SST. Understanding how the heat transfer from the surface metamorphose into modifications of the synoptic systems is well beyond the scope of this paper. We will finally limit our scope of study to the first day of diurnal warming and observe the wind profile response as flow crosses over diurnal warming of SST. By only focusing on the first day of diurnal warming, we are unaffected from the influence from secondary feedbacks (wind amplification within storm systems). This allows us to analyze the PBL depth scales of the initial dSST-wind coupling and what mechanisms are initially responsible for the changes to the near-surface wind speed.

6.2 Momentum Budget of Trajectories

While there is extensive evidence that shows SST perturbations are well correlated to changes in the wind stress for flow across the perturbation gradients, it is also noteworthy that the exact dominant mechanism responsible for this coupling is being debated. The pressure gradient dominant mechanism was first described as a mechanism for low-level winds and SST coupling by *Lindzen and Nigam* [1987] while looking at low level flow in the PBL and convergence of winds from pressure gradients generated by the SST gradients. Their simple one-layer model of the cumulus boundary layer showed that the horizontal convergence acts to reduce the the horizontal pressure gradients near the equator. However, *Hashizume et al.* [2002] and *Xie* [2004] pointed out that the pressure gradient mechanism does not explain the enhancement of winds over the warm water where gradients and wind enhancements are 90° out of phase. Conversely, the vertical mixing of momentum theory, which was first suggested by *Wallace et al.* [1989], would describe the enhancement of winds over an anomalously warmer SST from the intensification of vertical mixing from the warmer sea surface. The vertical mixing theory mechanism has been observed in several recent modeling studies; for example, *O'Neill et al.* [2010] examined the dynamical response from a mesoscale SST perturbation along the Agulhas Return Current during a 1-month long, southern hemisphere wintertime WRF simulation. Their simulations indicated that the SST-induced heat anomalies incited a vertical turbulent redistribution of momentum along with the anomalous pressure gradients to accelerate the wind toward warmer water and vice versa. The monthly averaged wintertime surface wind speeds were roughly 10 m/s to 16 m/s in the southern region of their domain. For the downwind momentum budget, they observed that both the turbulent momentum mixing and pressure gradient forces were important in the SST-induced surface wind speed response because they were of the same sign and roughly same magnitude. In addition, the crosswind acceleration showed a clockwise direction perturbation due to the Coriolis force that acted along with the crosswind pressure gradient perturbations. However, they also showed that the turbulent stress divergence perturbations were not spatially collocated with the downwind wind stress perturbations (or accelerations of wind speed over warm water); thus, the role of the turbulent stress divergence perturbations were two fold: first, to exchange momentum between lower and upper portions of the marine boundary layer, altering the wind shear. Second, exert an anomalous surface drag as a result of the pressure gradient forcing. *Kilpatrick et al.* [2014] showed that the wind profile in WRF

simulations can also be explained primarily by the interaction of the turbulent stress divergence in reaction to the SST front in reference to the Coriolis force and the pressure gradient force (disturbance of Ekman balance). The vertical changes to turbulent stress divergence produced a drag in the mid levels of the MABL that decelerated winds and accelerated the winds at the surface, that proved consistent with the vertical transport of momentum mechanism.

Combining the methodologies of *O'Neill et al.* [2010] and *Kilpatrick et al.* [2014], we compute the mean momentum budget for a set of ground-based trajectories encountering two areas of interest in order to understand the boundary layer responses. In order to compare to the results of *O'Neill et al.* [2010] and *Kilpatrick et al.* [2014], we selected specific trajectories that experience a cold-to-warm dSST transition and a warm-to-cold transition on the first day of diurnal warming (to reduce the influence of secondary feedbacks with the synoptic systems). For the cold-to-warm case, the ground-based trajectories flow towards the west and turn northwest as they encounter diurnal warming (that is, the trajectories go from cooler to warmer water) (Figure 6.8). The trajectories consist of advected parcels of air driven purely by the speed of the near-surface wind within the diurnally varying simulation. The trajectories are then collocated to the nearest grid point to create a Lagrangian time series of boundary layer data within 2 km of the surface (Figure 6.9). At roughly the same time, there is a 1.5 m/s local increase in the surface winds adjacent to the diurnal warming between 50°W and 46°W just after local sunset. The wind anomaly is initially generated at the surface and grows to the height of the boundary layer. This particular band of positive wind anomalies persists for an additional 24 hours. We calculated the terms of the momentum budget following *O'Neill et al.* [2010] in natural coordinates because of the non-zonal synoptic flow of the trajectories selected. The terms of the momentum budget in the downwind and crosswind directions are

$$V\frac{\partial V}{\partial s} = (-w\frac{\partial V}{\partial z} - \frac{1}{\rho}\frac{\partial p}{\partial s} + \boldsymbol{F}\cdot\hat{s}) \tag{6.1}$$

$$V^2\frac{\partial \phi}{\partial s} = (-wV\frac{\partial \phi}{\partial z} - fV - \frac{1}{\rho}\frac{\partial p}{\partial n} + \boldsymbol{F}\cdot\hat{n}) \tag{6.2}$$

where (s, n, z) are the local downwind, crosswind, and vertical coordinates, respectively; V is the wind speed; ϕ is the meteorological wind direction referenced from the eastward coordinate; w is the vertical velocity, f is the Coriolis parameter, ρ is the density of the air; p is the air pressure; and

$\boldsymbol{F} \cdot \hat{s}$ and $\boldsymbol{F} \cdot \hat{n}$ are the projected components of the zonal and meridional Reynolds vertical turbulent stress divergence terms. Each of these derivatives is calculated in downwind and $k \times \boldsymbol{V}$ directions. Figure 6.10 shows each of the terms of the cross-wind and along-wind momentum budget for the trajectories in Figure 6.8. Note that negative change in the advective tendencies corresponds to a positive wind acceleration. The local wind acceleration in the time series is primarily the result of the along and cross-flow anomalous pressure gradient generated by the diurnal warming as its time series correlates well to the increase in the meridional wind component (Figure 6.8), while the downwind vertical advection is relatively small and turbulent stress divergence only acts as a relatively small drag on the perturbation flow in the along-wind direction. Note that the influence of the turbulent stress divergence term is delayed compared to the pressure gradient effect and that it acts as a possible restoration to Ekman balance given the simultaneous decrease in the Coriolis force and advection. The vertical advective terms are small compared to the forcing of the pressure gradient, Coriolis, and turbulent stress divergence as is consistent with *Kilpatrick et al.* [2014] and *O'Neill et al.* [2010]. Changes of the forces at play are initiated at the surface and, with the exception of Coriolis, are largest in the lower 1—1.5 km of the boundary layer.

The reversal of these dominant forces is also observed for trajectories flowing away from the diurnal warming. These trajectories are flowing across the diurnal warming to the north coincident with a large area of negative wind anomalies. The surface meridional wind component is the result of flow opposite of the anomalous pressure gradient enhanced by the reduction in drag by the turbulent stress divergence below 400 m and the reduction in the Coriolis forcing. We also noted a decoupled surface wind deceleration and a mid-level acceleration that is likely related to a decoupling of the boundary layer as it advances towards a higher wind speed regime.

These coupled simulations suggest that for the initial dSST-wind coupling, the surface pressure gradient mechanism dominates over the turbulent stress vertical mixing of momentum. We expect limited vertical motion because the diurnal warming takes place under a statically stable and capped boundary layer and limited mechanical mixing as a result of low wind speeds. We calculated the stability parameter (Obukhov length L divided by the height of the wind observation z) to give us a measure of the length scale of convective vs shear driven turbulence:

$$L = \frac{u_*^3 T_v}{kgQ_{v0}} \tag{6.3}$$

It is not until after sunset that the stability parameter becomes negative, destabilization of the atmosphere occurs, and we expect more influence from convective-driven turbulence. In these two examples, we have shown that the flow across the diurnal SST gradient is physically consistent with a pressure gradient enhancement, but that in this particular case, the vertical mixing of momentum was less important until a destabilization of the atmosphere allowed more convective overturing.

While the modeling study here did not fully explain the dynamical processes relating to the influence of the diurnal SST variability on near-surface winds, it does suggest implications that future SST-wind coupling studies should consider; first, this work suggests we need a better understanding of the role of marine boundary layer stability and the coupling of SST and wind anomalies. If the static stability of the atmosphere (or a large temperature inversion cap) exists that prevents a significant mixing of the classic logarithmic wind profile, would the vertical mixing of momentum be a dominant mechanism? Second, future studies should also consider whether the mean synoptic flow is independent of SST perturbations. We do not expect the weak wind conditions in which we are working to be an inhibiting factor because many of the SST-wind coupling observations have been made in the tropics where the trades are equally weak. Rather, we have simulated wind-SST interaction where the SST is already fully dependent on spatial distribution of the synoptic flow. It is possible that the mean wind-SST interaction described herein is completely dynamically different than wind SST-perturbation coupling across western boundary currents and/or tropical instability waves and thus longer simulations would need to be performed to understand the mean wind field impacts of diurnal-SST and wind coupling.

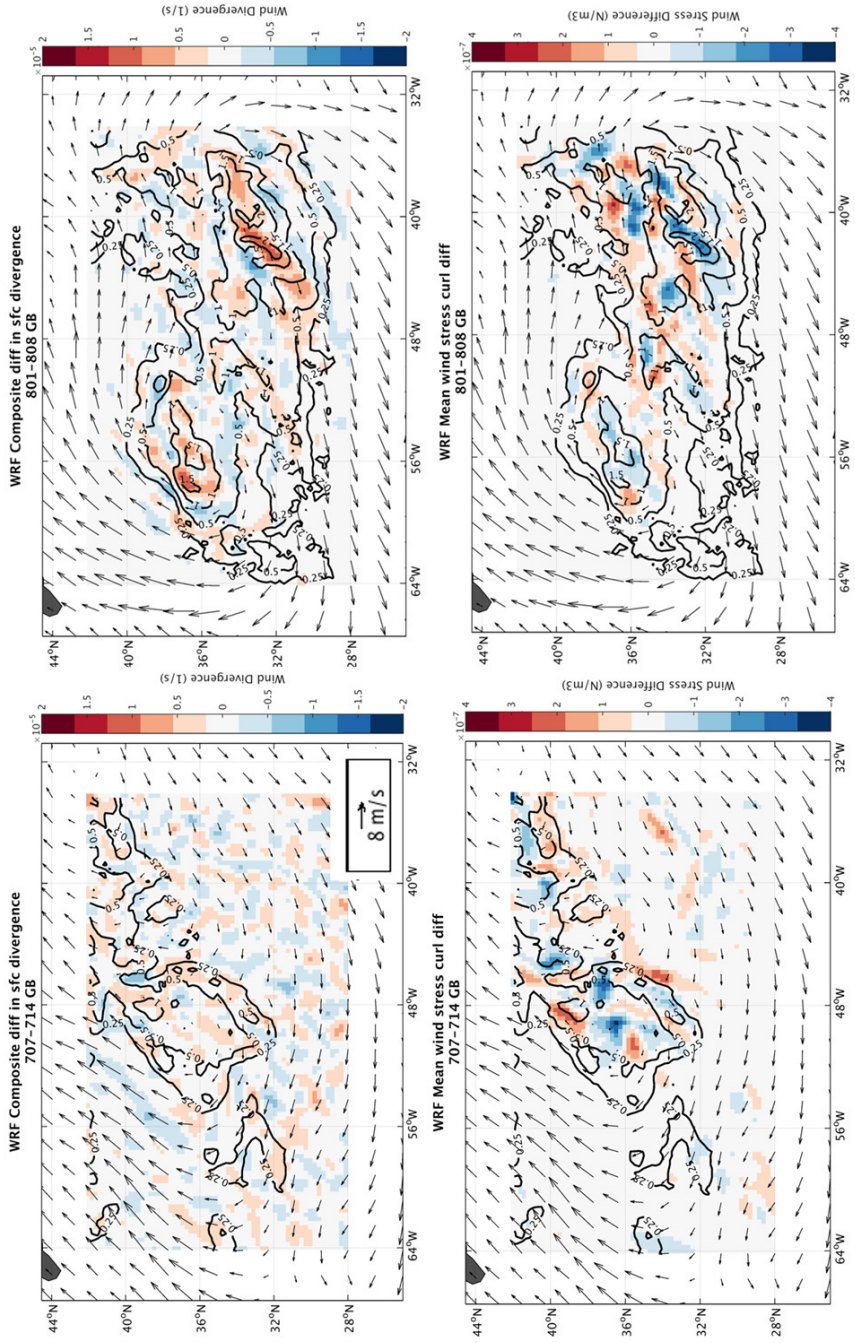

Figure 6.1: Mean differences in wind stress curl (left column) (N/m3) and surface wind divergence (right column) (1/s) over 7-14 July, 2014 (top row) and 1-8 August, 2012. The average magnitude of diurnal warming is contoured and mean wind vectors from the diurnally varying simulation are shown.

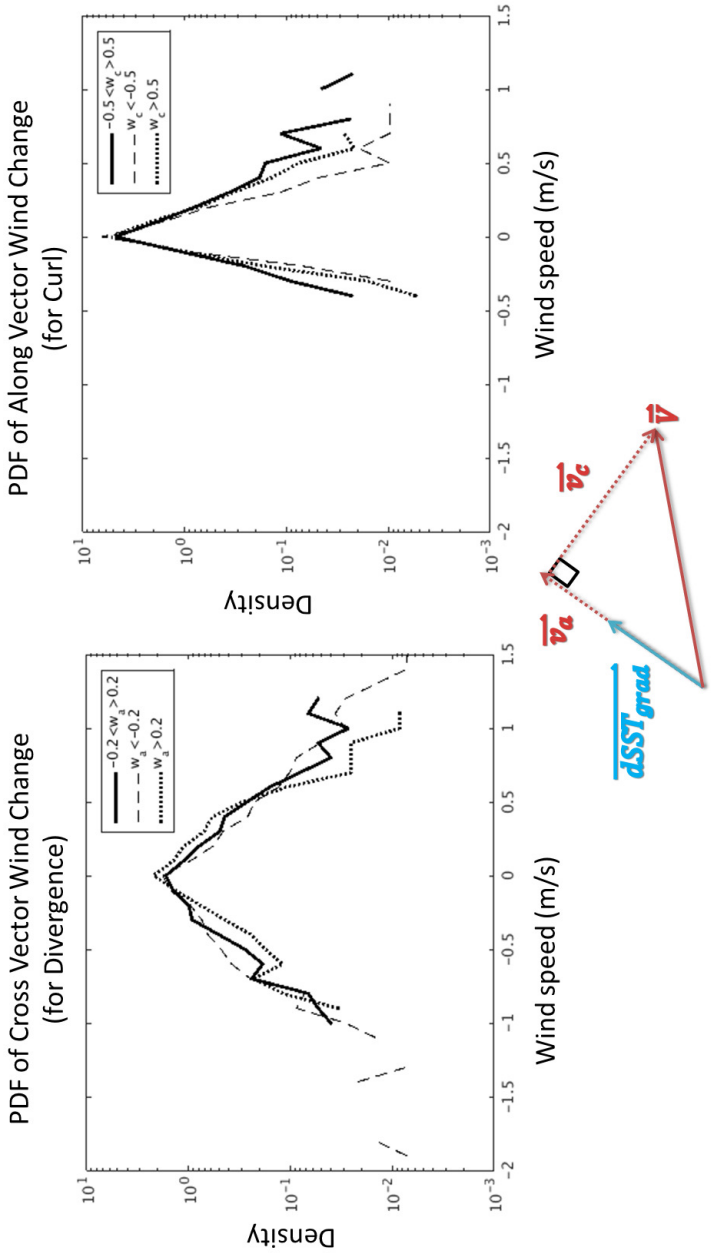

Figure 6.2: Probability distribution functions of the projected wind vectors onto the (left) k × dSST gradient vector and (right) along dSST gradient vector. For the probability distribution functions plotted on the left, the solid line represents the distribution of the cross-dSST gradient vector when the along-gradient vector component is approximately zero, the long dashed line is when the along-gradient component is negative, and the short dashed line is when the along-gradient component is positive. The same is true for the right figure when the along and cross-gradient vector components are interchanged.

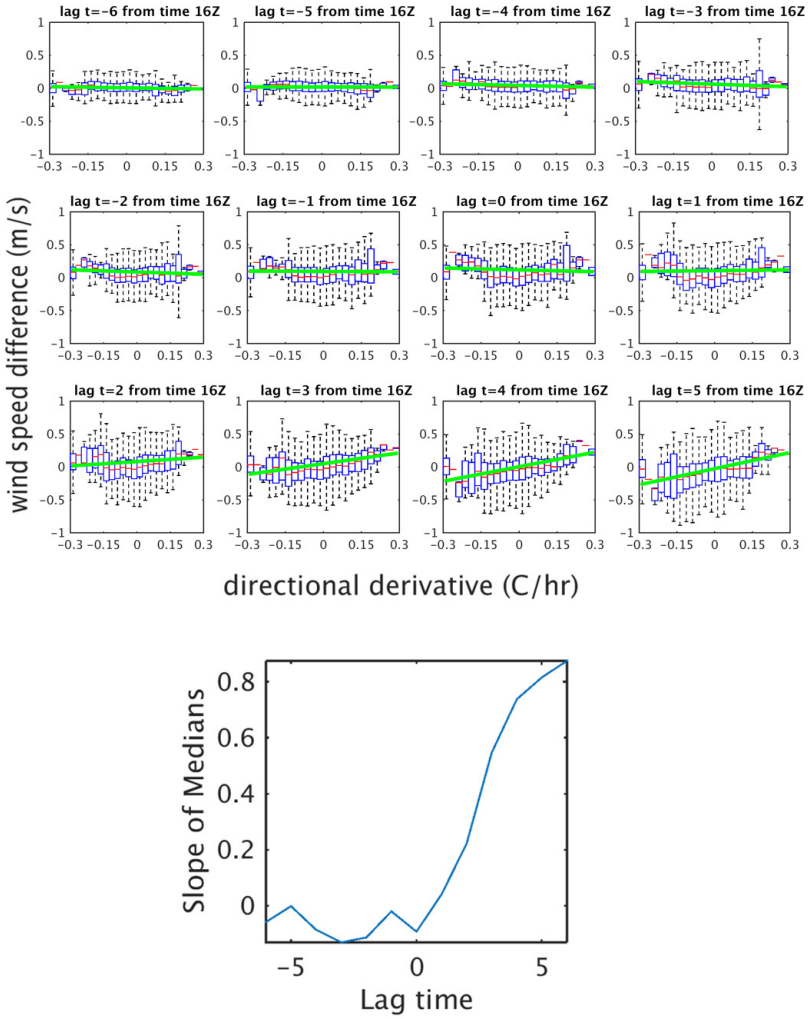

Figure 6.3: (Top Panels) Box plots showing the changing distribution of wind speeds (m/s) as a function of lag from 16Z on 7 July, 2014. A lag time $t = -6$ means the wind speed differences from 10Z are plotted relative to the locations of the diurnal warming gradient occurring at 16Z. The box plots are binned by the magnitude of directional derivative (magnitude of the wind in the direction of the dSST-gradient) from ocean warming occurring at 16Z. The length of the boxes indicates the magnitude of the 25th and 75th quartiles, the red line inside the box is the median value. The green line is the slope of a line fitted to medians of the first and last six boxes of the plot. (Bottom plot) The magnitude of the slope as a function of lag time.

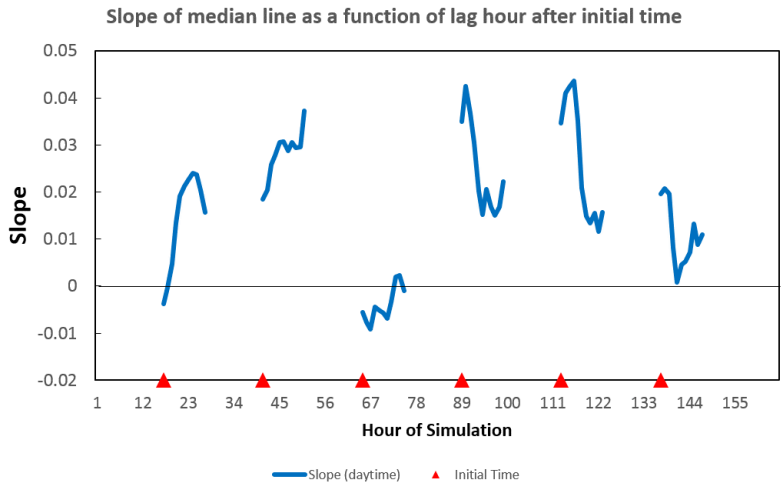

Figure 6.4: Tendency of wind-dSST coupling as a function of time after diurnal warming has occurred on each day of the simulation from lags = 0 to 10 hr. Each segment represents the slope of the line fitted to the median of the wind speed distribution (see Figure 6.3) as a function of hour after the initial time (red triangles). The initial time represents the time at which the directional derivatives were calculated. For clarity, the first segment plotted here is the replication of a portion of the slop tendency plotted in Figure 6.3.

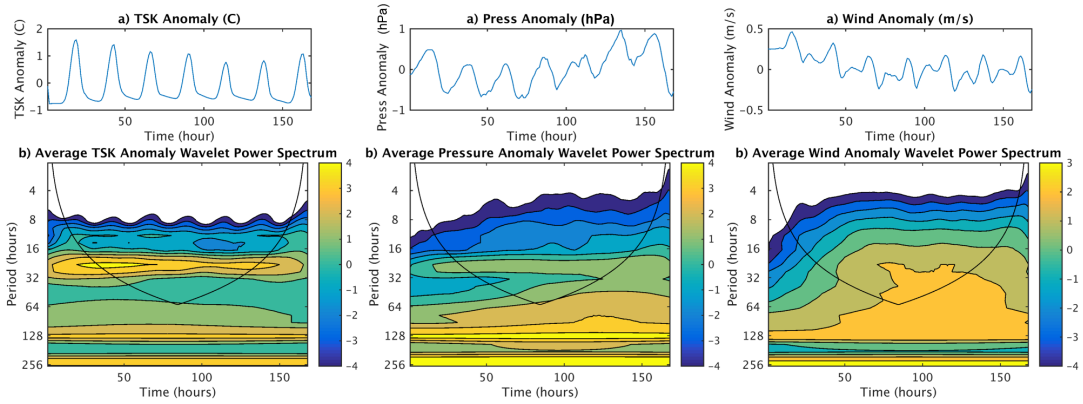

Figure 6.5: Mean (top row) anomaly time series and (bottom row) wavelet power spectra of the (left) magnitude of diurnal warming (K), (middle) sea level pressure (hPa) difference, and (right) wind speed difference (m/s) between the diurnally varying and daily-constant simulations for 1-8 August, 2012.

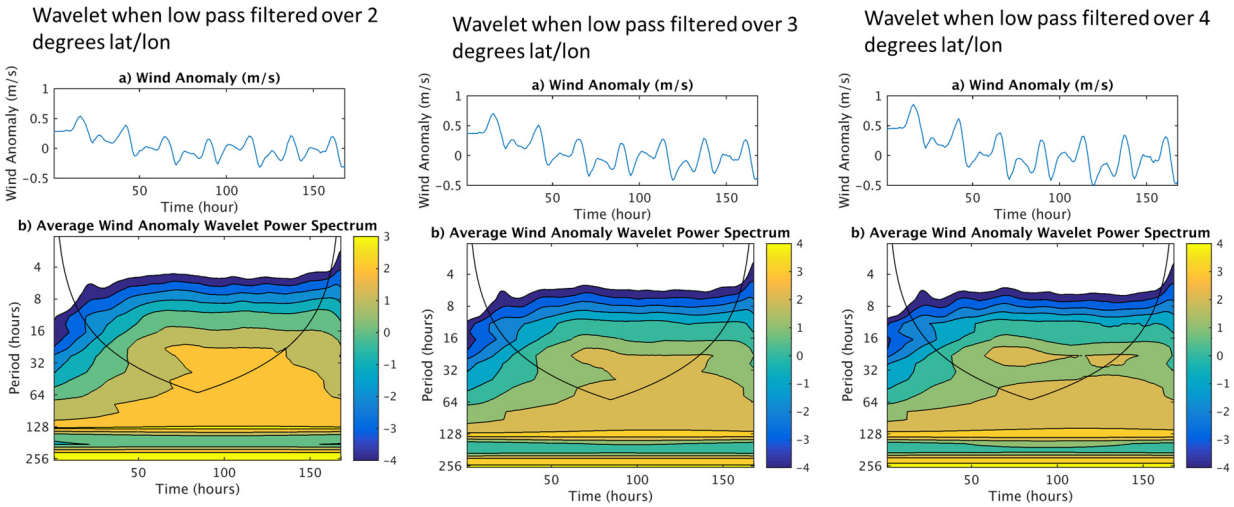

Figure 6.6: Same as Figure 6.5 for wind differences (m/s) that have been spatially filtered to reduce variability with wavelengths smaller than (left) 2°, (middle) 3°, and (right) 4° latitude and longitude.

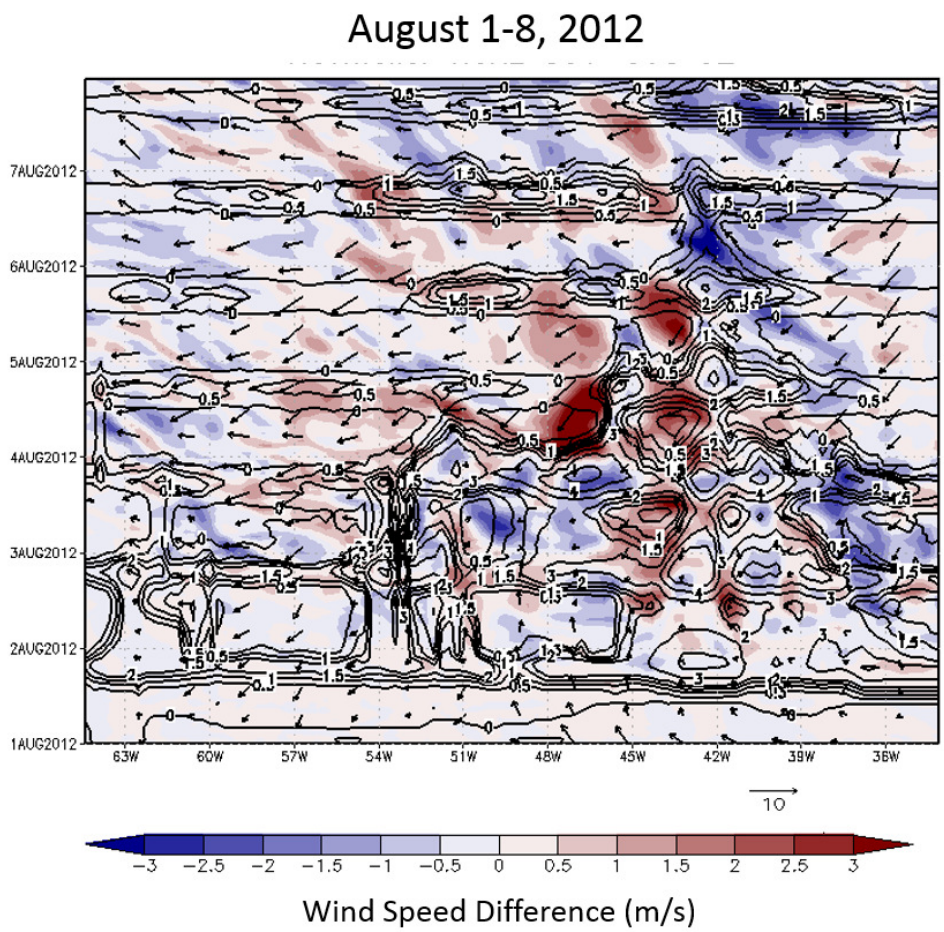

Figure 6.7: Hovmöller diagram of the diurnal warming (contours, K) and differences in wind speed (shaded, m/s) and wind vectors occurring in the diurnally-varying simulation for the 1-8 August case study at 32°N.

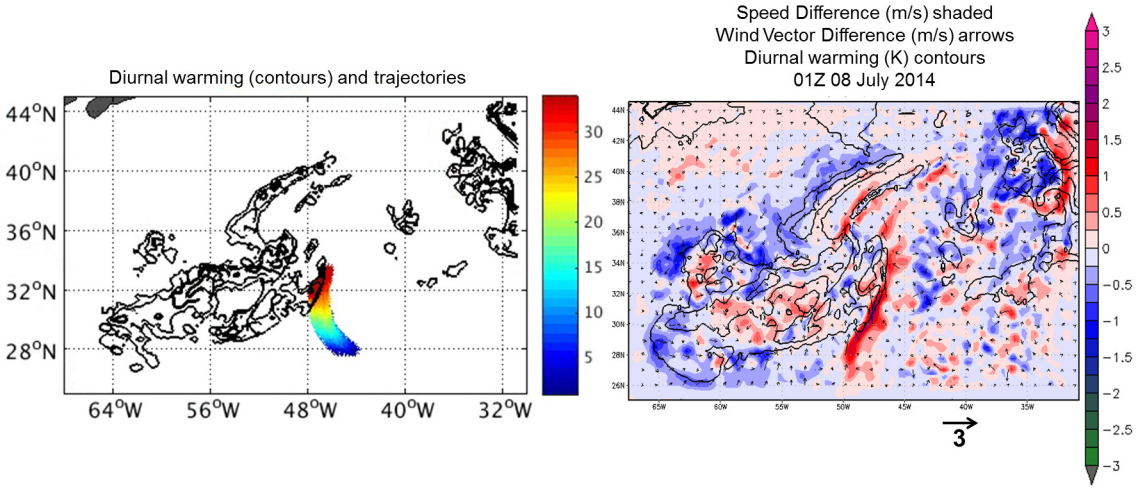

Figure 6.8: (Left) positions of surface-based trajectories as a function of hour into the July 2014 simulation over contoured diurnal warming greater than 0.5 K and (Right) the changes in wind speed (shaded), vector wind difference (m/s), and the magnitude of diurnal warming (K) (contoured every 0.25 K) at 01Z 8 July.

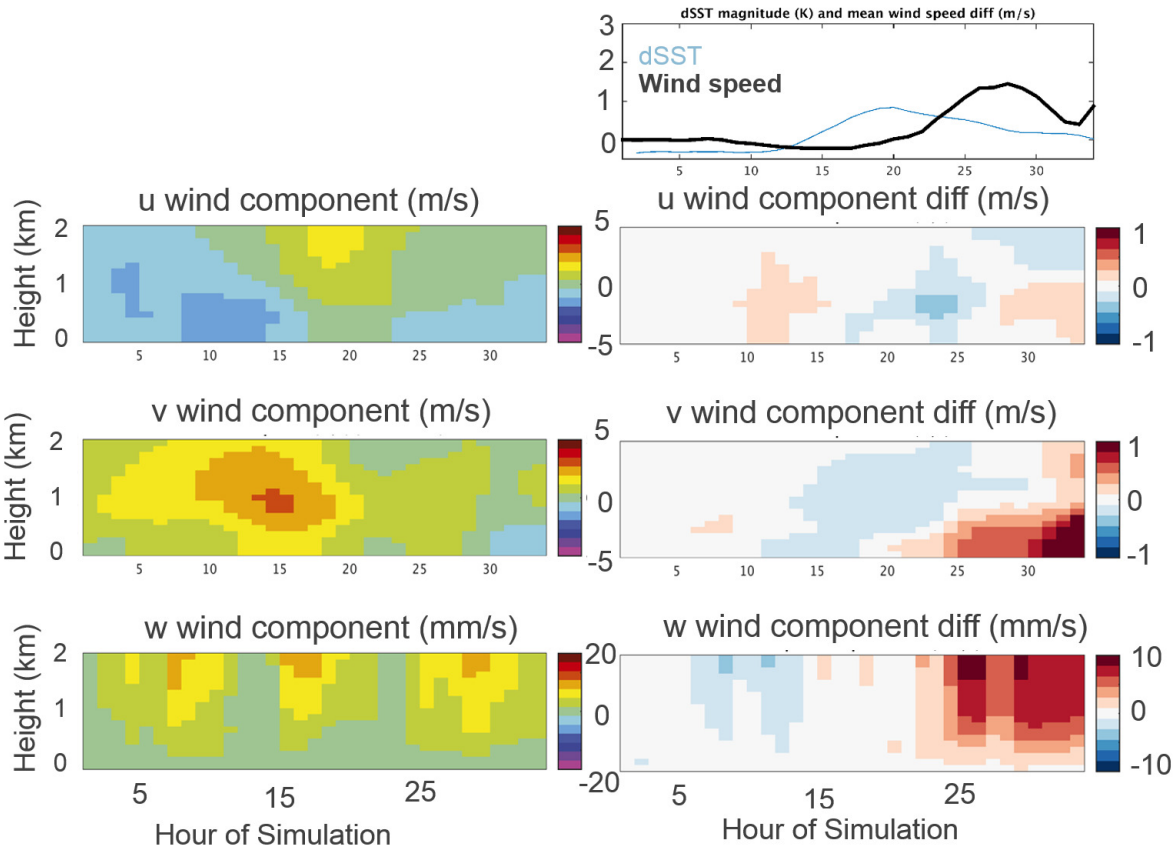

Figure 6.9: (Right top) Mean amplitude of the diurnal warming (K, blue line) and wind speed difference (m/s, black line) between the diurnally varying and daily-constant trajectories. (Left column) Values in the daily-constant simulation and (right column) differences between daily-constant and diurnally varying simulations in the U (m/s) (second row), V (m/s) (third row), and W (mm/s) (fourth row) components of the wind vector within the lowest 2 km for trajectories in Figure 6.8

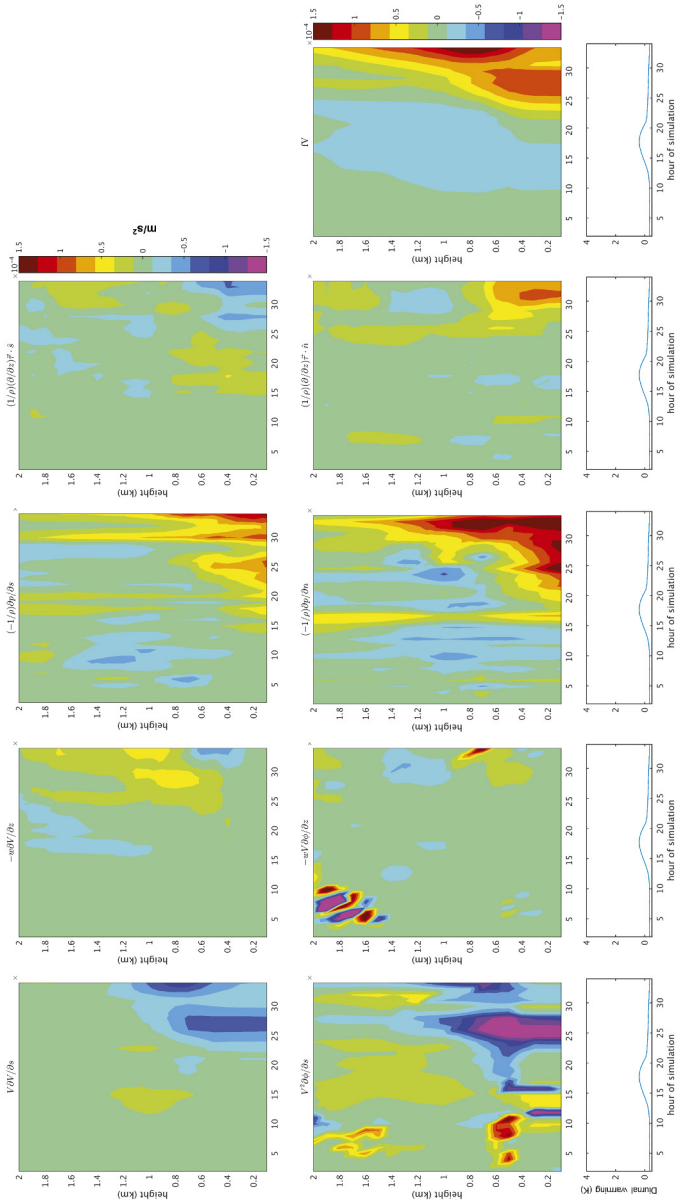

Figure 6.10: Differences in the terms of the marine boundary layer momentum budget; a) along-wind advective tendency, b) along-wind vertical advection, c) along-wind turbulent stress divergence, d) along-wind pressure gradient force, e) cross-wind advective tendency, f) cross-wind vertical advection, g) cross-wind turbulent stress divergence, h) cross-wind pressure gradient force, and i) Coriolis force in units of m/s^2 for trajectories flowing across warm to cooler dSST. The average time series magnitude of diurnal warming (K) is plotted in the bottom row for reference.

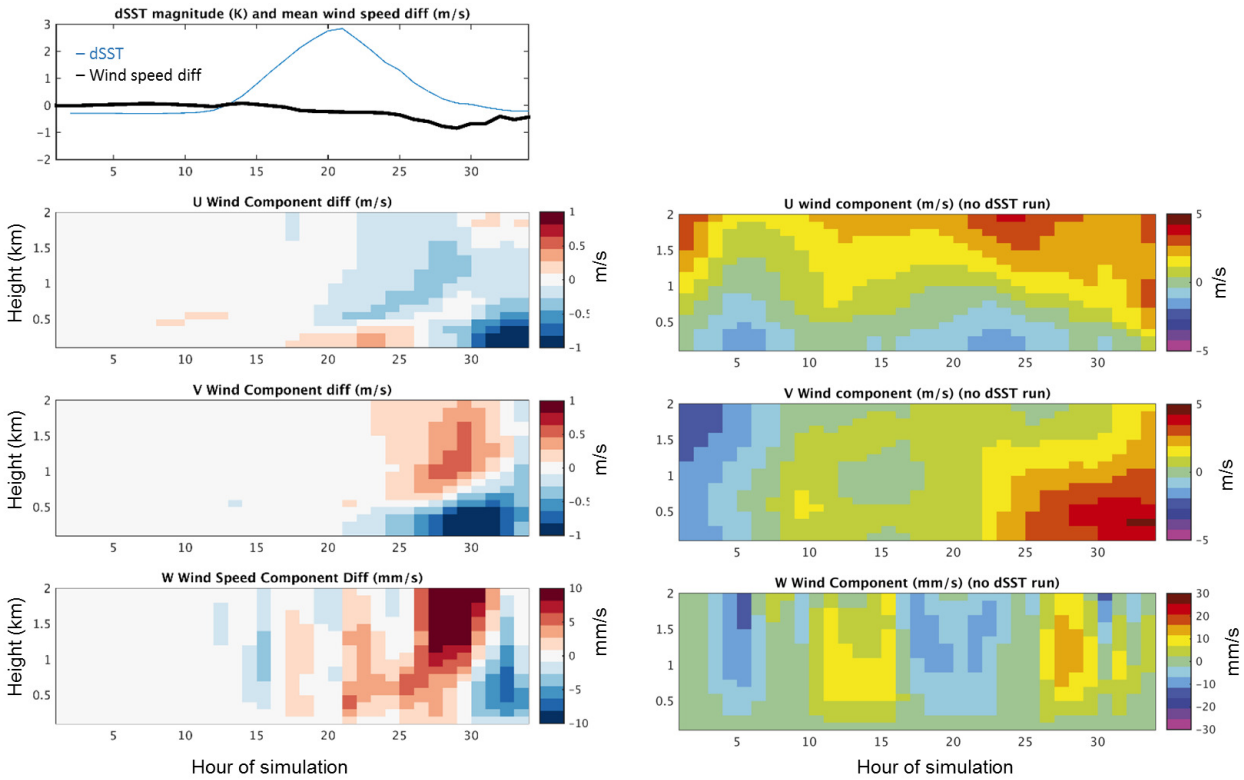

Figure 6.11: Same as Figure 6.9 for trajectories flowing from warmer to cooler SST

.

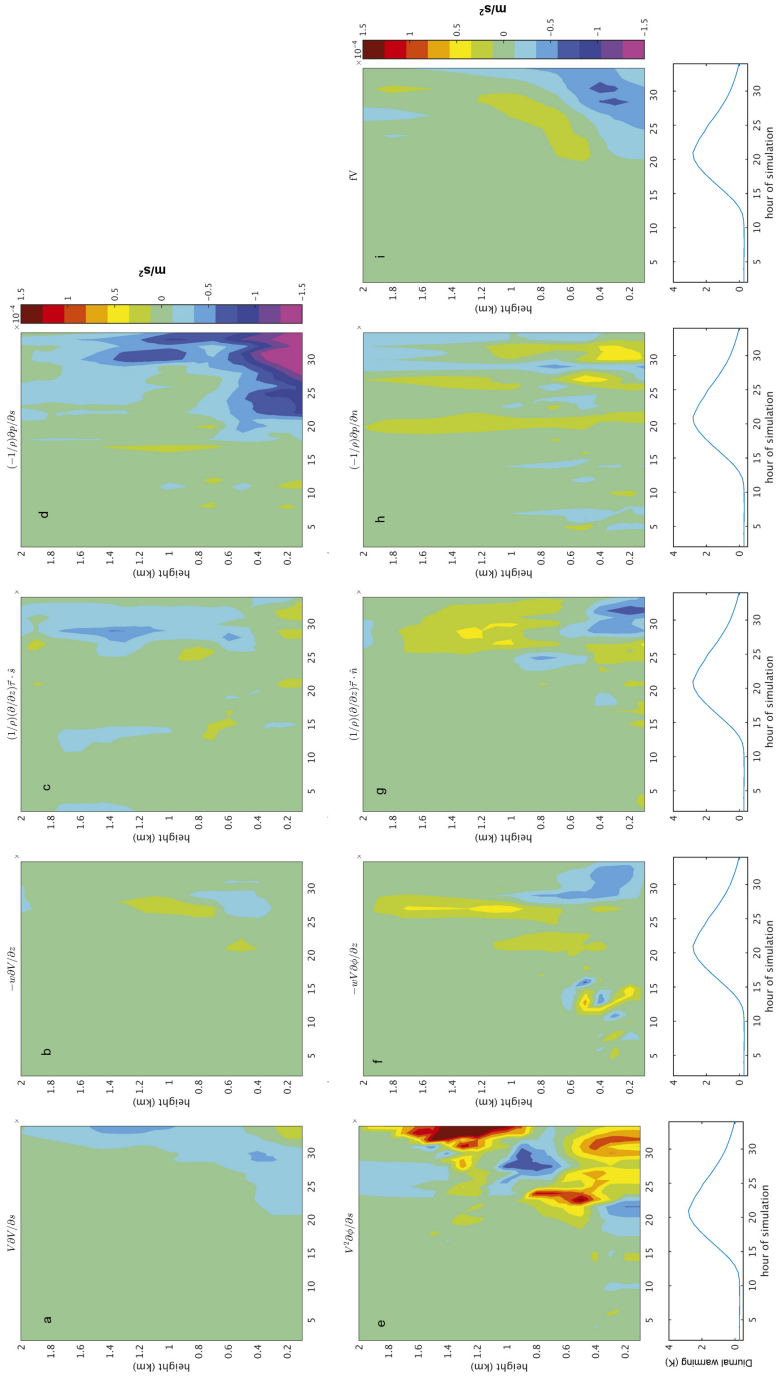

Figure 6.12: Same as Figure 6.10 for trajectories flowing from warmer to cooler SST.

CHAPTER 7

ONE-WAY VERSUS TWO-WAY COUPLING ON THE DIURNAL CYCLE OF SSTS

The use of coupled atmosphere and ocean models for understanding of SST-heat flux feedbacks have been shown to improve the intraseasonal variability of atmospheric phenomena such as the Madden-Julian oscillation (MJO) [e.g. *Shinoda and Hendon*, 1998] but could underestimate the SST response if dynamics of the upper ocean are not accounted for [e.g. *Inness et al.*, 2003]. The computational cost of modeling the upper-ocean structure can be significant; *Bernie et al.* [2005] and *Pimentel et al.* [2008] showed that in order to reproduce 90% of the diurnal variability during the suppressed phase of the MJO, a global coupling frequency of 3 h or less is required with an ocean vertical resolution of 1 m or greater. However, this study, using a regional model, has shown that diurnal fluctuations in the SST have paramount consequences in the diurnal atmospheric boundary layer dynamics and supports the necessity of coupled models in simulating atmospheric diurnal variability.

As with the research described herein, many of these studies [e.g. *Danabasoglu et al.*, 2006; *Brunke et al.*, 2008, and references herein] justify the use of coupled models for better representation of the intraseasonal variations in SST and atmospheric responses by demonstrating the improvement to mean SST, boundary layer depth, and vertical heat and momentum fluxes. In this section, we describe the potential implications of "one-way'' versus "two-way" wind-dSST coupling in the WRF model. A two-way coupled model allows for the diurnal warming at time t to modify the boundary layer and affect the local wind speed that, in turn, influence the subsequent diurnal cycle of SSTs at time $t + 1$ throughout the simulation. A one-way coupled model only allows the ocean-to-atmosphere feedback, without using the modified the fluxes and winds for the next time step. A one-way approach is very common for diurnal warming studies when external data that lack strong air-sea coupling (usually reanalysis data that use daily mean SST) are used as forcing for the diurnal warming amplitude [*Noh et al.*, 2011]. To our knowledge, this is the first study to quantify the impact of the coupled winds on the amplitude of the diurnal warming.

At each concurrent time step in both two-way and one-way coupled simulations, the diurnal warming is computed and the SST with diurnal variability is sent to the surface flux routine and outputs are saved. However, for the one-way coupled run, after outputs are saved, all key variables are calculated once more using the foundation SST (MUR in this case). These secondary calculations are saved in history and used for the next time step's calculations. The comparison is done for the July simulation only.

Figure 7.1 shows the mean magnitude of diurnal warming (in K) over the entire domain for the one-way coupled simulation (red) and two-way coupled simulation (green line) for the July 7-14 period. On average, both models simultaneously produce diurnal warming each day at the same time. However, the mean two-way coupled simulations have an overall smaller peak in amplitude of warming and a shorter duration of the diurnal cycle each day. The mean reduction in peak diurnal warming on July 7th is 0.3 K.

Hourly differences during the peak of the diurnal warming can exceed 1 K (Figure 7.3), especially where diurnal warming is >2 K in the two-way simulation. An analysis of the temporal errors (not shown) indicates that the peak differences between the one-way and two-way simulations occurs 1-2 hours after peak heating has been reached in the two-way simulation. For a strongly stable atmosphere away from dSST gradients, a higher peak in the diurnal warming would also mean the diurnal warming would take a longer period of time to erode overnight. Diurnal warming is non-linearly related to surface wind speeds, and therefore can be sensitive to errors especially in low wind conditions. Figure 7.2 shows the differences in the wind speeds between the one-way and two-way coupled simulations versus the peak diurnal warming. When the diurnal warming is larger in the one-way simulation, the winds are more likely to be smaller. The mean wind speed is reduced in the one-way simulations for wind speeds lower than 3 m/s. As we saw in the comparison section, the ZB algorithm over-predicts the diurnal warming; using the one-way coupled model would further exacerbate the over-prediction particularly with extreme heating events.

Figure 7.4 shows the latent heat flux differences between the one-way and the two-way coupled simulations. The differences of the latent heat fluxes are well correlated to the differences in wind speed between the diurnally varying and daily constant simulations as well as the difference in magnitude of the dSST between the two simulations (contours). We can deduce that the latent heat flux difference is the compounded circular result of flux-to-wind feedback and wind-to-dSST

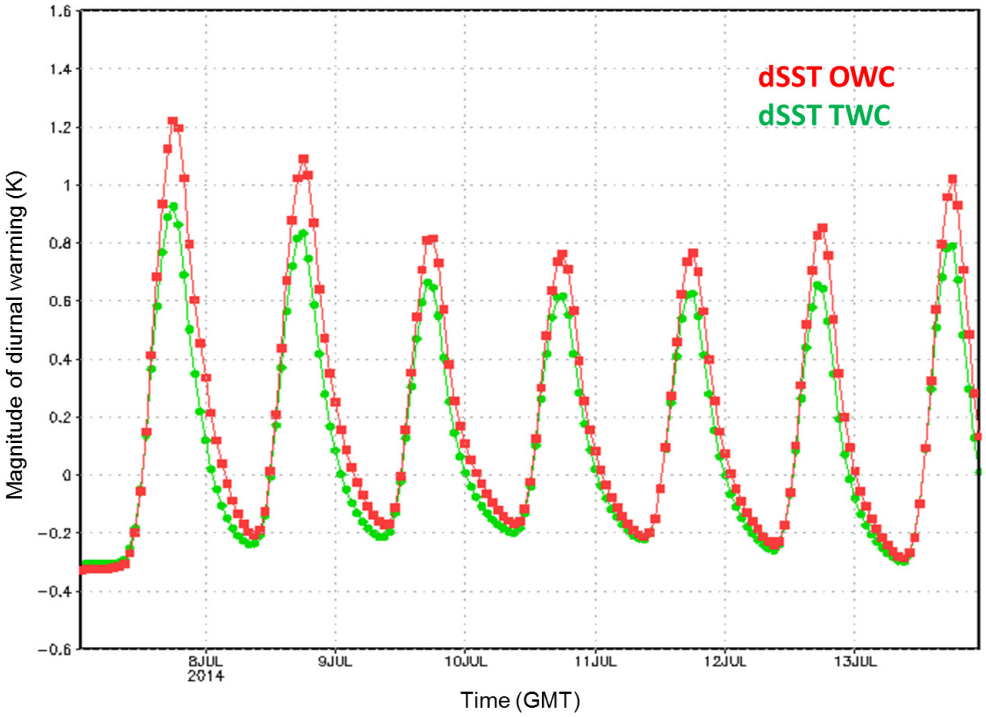

Figure 7.1: Mean diurnal warming (K) for the one-way (red line) and two-way (green line) coupled WRF simulation for 7-14 July, 2014.

warming feedback. On average, the latent heat fluxes between the two simulations differ by roughly 10 W/m^2 but can vary up to 40 W/m^2 in places where the differences in diurnal warming exceed 1.5 K. Note that the largest latent heat flux increase due to diurnal warming in the two-way simulations is on the order of 60 W/m^2 [*Fairall et al.*, 1996a; *Ward*, 2006; *Weihs and Bourassa*, 2014]. Thus, as a consequence of uncoupling the ocean skin temperature to the atmosphere on subsequent time steps, the peak magnitude of diurnal warming has doubled and the resulting changes in fluxes increased by 67% in extreme cases. The "extra heat" in the one-way coupled simulation is not rectified by the atmosphere in concurrent time steps without and SST and flux feedback. It creates a slightly more unstable atmosphere as indicated by an increase in the Monin-Obukhov length.

Through this test, we have determined the impact of a coupled atmosphere-dSST model by quantitatively examining the changes to the amplitude of warming and the latent heat fluxes. In extreme cases, we have severely overestimated the magnitude of diurnal warming and the resulting fluxes in a one-way coupled model. *Schiller and Godfrey* [2005] coupled a sublayer 1-D ocean model to an atmospheric boundary layer model and found that the coupled and uncoupled models performed equally in producing sublayer SSTs and differed from observations (at depth) by only 0.2 K. Thus, when the skin temperature differences exceed 0.2 K, we would expect a more significant change in the fluxes as modeled in this study. If we desire to fully understand the influence of the diurnal warming on the atmosphere, we must consider a fully coupled system wherein the changes to the surface fluxes, skin SST, and wind speed are all allowed to influence each other.

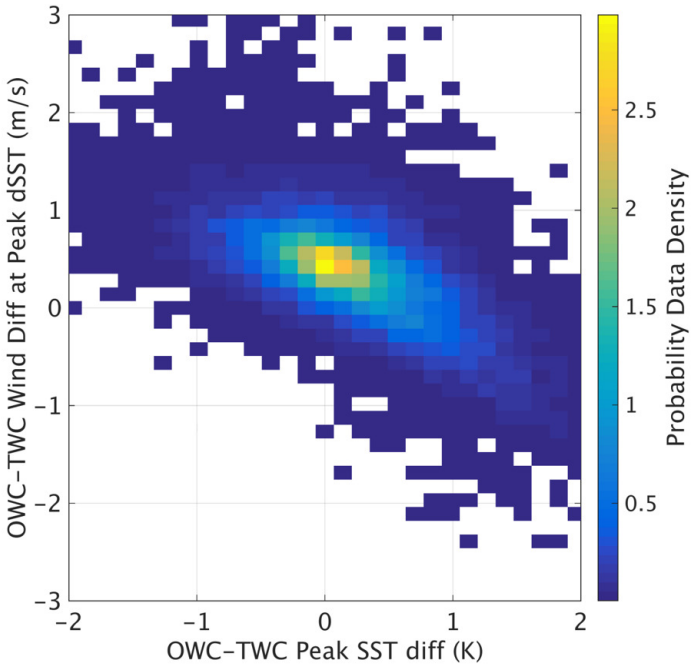

Figure 7.2: One-way minus two-way coupled differences in wind speed (m/s) at peak diurnal warming versus one-way minus two-way coupled peak diurnal warming (K) for the July simulation. The shaded values indicate data density of the scattered data.

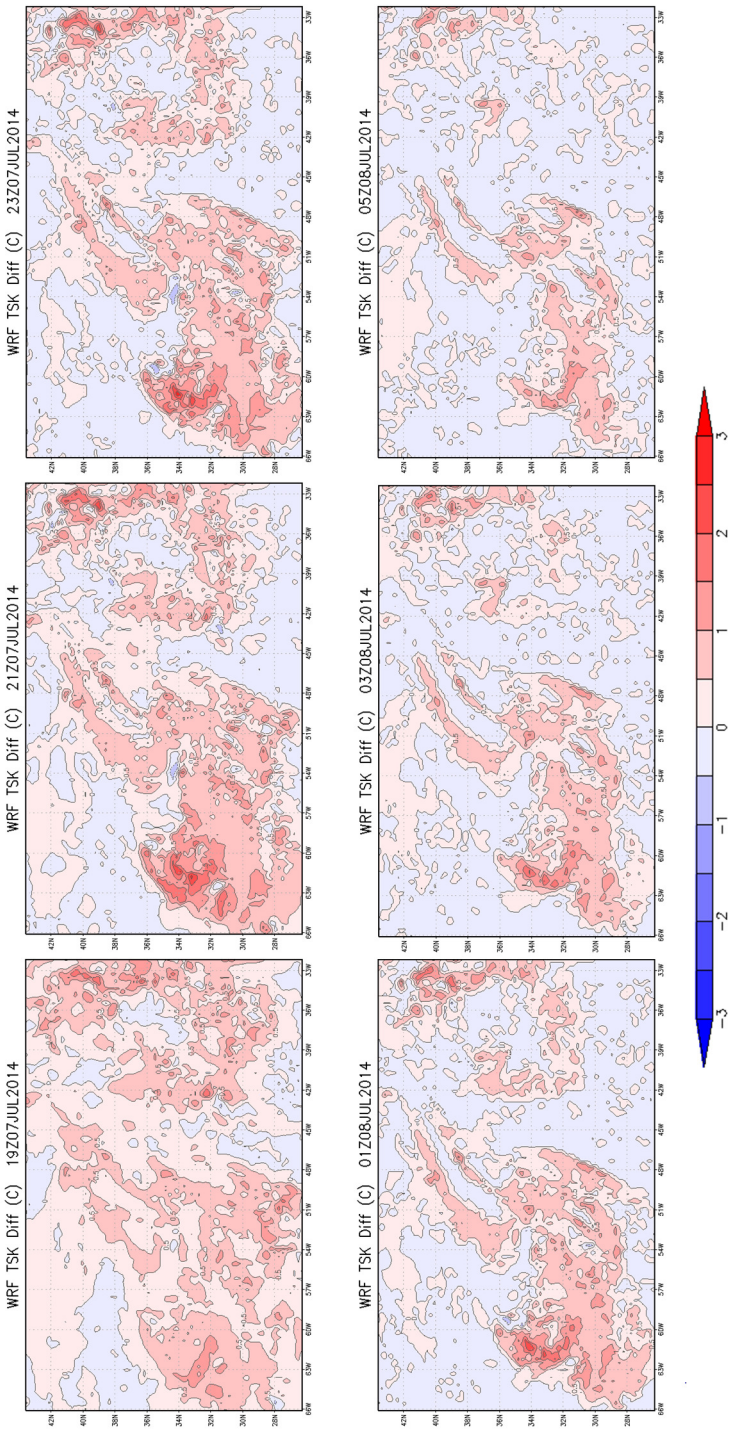

Figure 7.3: One-way minus two-way coupled differences in the amplitude of diurnal warming (K) at 19Z 7 July (top left), 21Z 7 July (top middle), 23Z 07 July (top right), 1Z 8 July (bottom left), 3Z 8 July (bottom middle), and 5Z 8 July (bottom right).

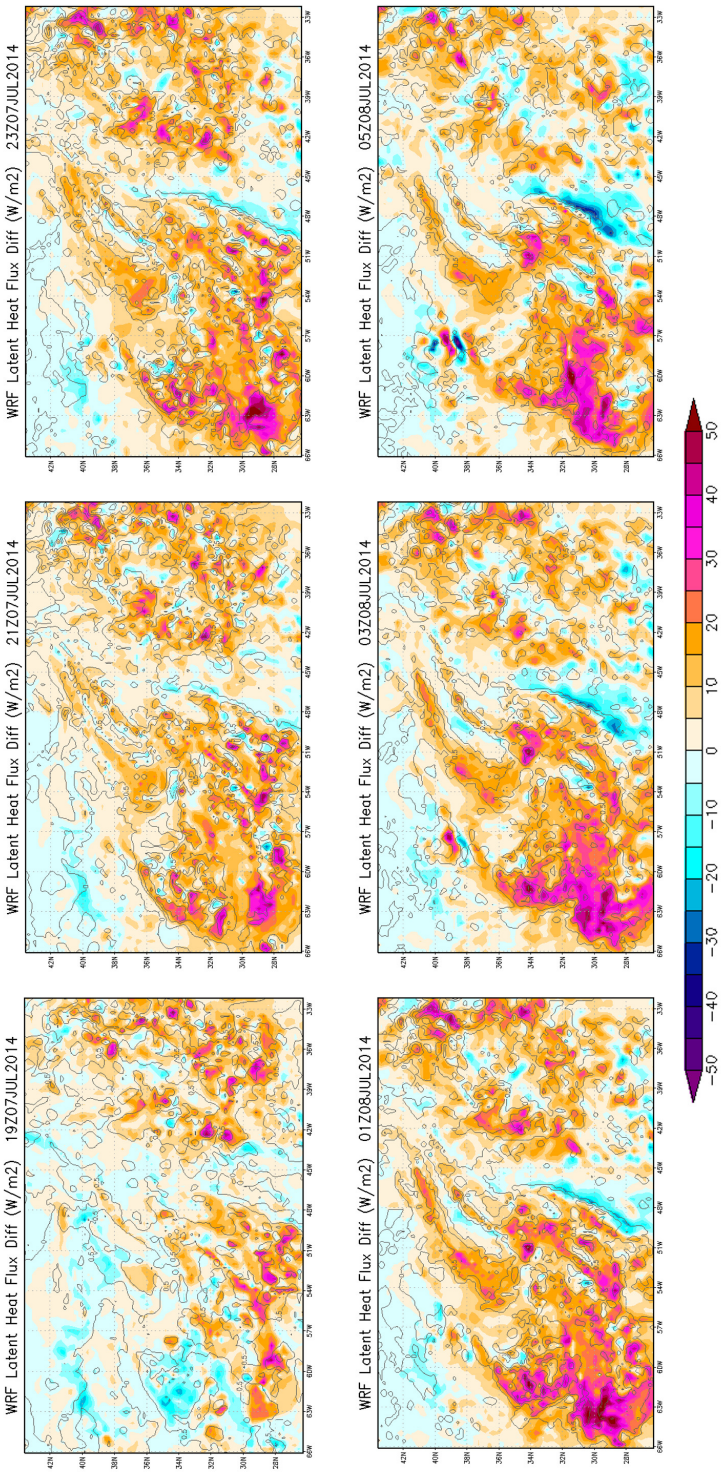

Figure 7.4: One-way minus two-way coupled differences in the latent heat flux (W/m^2) at 19Z 7 July (top left), 21Z 7 July (top middle), 23Z 07 July (top right), 1Z 8 July (bottom left), 3Z 8 July (bottom middle), and 5Z 8 July (bottom right).

CHAPTER 8

CONCLUSIONS AND DISCUSSION

8.1 Summary

The effect of diurnal variations in SST on the marine atmospheric boundary layer is examined by computing case study simulations with a coupled regional atmospheric model and skin sea surface temperature algorithm. We compared simulations with and without SST diurnal variability for 2 week long periods in the northern central Atlantic in boreal summer. These simulations have shown that the coupled responses of diurnal variations in sea surface temperature have potentially paramount influences on both the regional synoptic weather as well as local changes to wind speeds and energy fluxes by air-sea interaction. Depending on different synoptic conditions, the amount of temperature change produced by diurnal warming of the ocean can be on the order of 3-4 K on daily time scales, and 1.5 K on a weekly average time scale. The amount of warming depends on the low surface wind speeds and high amounts of absorbed solar radiation in order to produce a stratified upper ocean. The ZB skin sea surface temperature algorithm responsible for the calculation of diurnal heating did overestimate the diurnal heating as compared to the GOES and SEVIRI data. However, the overestimation could be somewhat exaggerated by several factors such as the smoothing of the high resolution SST to the model resolution and the inhomogeneities between the input forcing of the model and the real world conditions measured by the satellite. We did, however, determine that the cool-skin portion of the algorithm produces a nighttime SST that is closer to observations than using a foundation temperature product.

We have gained valuable insight into the boundary layer variations from diurnal heating of the sea surface. The diurnal warming of the sea surface generates wind mean changes typically on the order of 0.5 m/s. Wind changes as a result of SST perturbations along western boundary currents and tropical instability waves are of similar magnitude. However, the diurnal warming also modifies the larger synoptic scale weather variability within the model. It is within these areas that we see the most dramatic changes to wind speed greater than 3 m/s as a result of storm track modification. In comparison to ASCAT-A data, some large wind observations were dramatically

reduced by 2 to 4 m/s and are more accurate compared to the satellite data. This could indicate that the changes to the storm track of the regional storm systems could be better simulated with diurnal variability but more robust statistics are needed to verify this.

The mean changes to the wind field (i.e. wind stress divergence and curl) did not appear similar to the perturbations that occur along western boundary currents and the like. We used a number of methodologies to determine whether mean diurnal warming gradients and wind anomalies were linked on diurnal time scales. By examining the distribution of the wind anomalies on the first day of the simulation as a function of the diurnal warming gradient, we observed a linear, but temporally lagged, wind-diurnal warming SST gradient coupling following the flow across the diurnal warming. This relationship was not evident in the wind speed distributions after the second day of the simulation. It is likely that the secondary feedbacks on the synoptic scale dominate the distributions after a given amount of time.

Because the diurnal warming and winds appeared to be coupled at least on the first day, we examined the mechanism by which the wind speed anomalies are likely to be influenced. The analysis of a momentum budget for trajectories crossing to and from the diurnal warming showed that the pressure gradient forcing was the dominant mechanism. The Reynolds stress divergence forcing was not a factor until after sunset, when the stability of the atmosphere decreased slightly.

Finally, we compared the amplitudes of diurnal warming in a one-way coupled simulation in which the diurnal warming is insensitive to dSST-modified flux forced winds. Rather, the computation of diurnal warming relies on the winds forced by the MUR foundation temperature at each time step. This is analogous to a study in which a diurnal warming model is forced with external atmospheric data (say, from reanalysis) and would be independent of dSST-related feedbacks. The one-way coupled simulation had a larger mean diurnal warming peak and longer duration of warming each day. The one-way coupled simulation results in extra heat flux from the diurnal warming that is not rectified by the atmosphere. The lowest winds appear to be reduced in the one-way coupled simulation. Because the diurnal warming is especially sensitive to changes in the low wind speeds, it produces a large amplitude increase in the cycle (an increase of 0.3 K, on average) that takes longer to erode overnight. Diurnal warming studies that wish to produce an accurate duration and amplitude of the diurnal cycle should strongly consider using a coupled model in order to allow heat flux related feedbacks to the near surface and marine boundary layer.

8.2 Future Work

The case studies presented herein give an intriguing, but preliminary, inside look into the short term marine boundary layer effects in response to the diurnal warming of the ocean surface. This methodology could be improved upon by selecting a skin sea surface temperature model that includes a responsive diurnal warm layer depth. *Takaya et al.* [2010] has made such refinements to the ZB algorithm and it could be implemented into the WRF physics packages as an alternative diurnal warming model. Other studies have shown success in coupling WRF to a mixed layer ocean model [e.g. *Noh et al.*, 2011] but require a vertical resolution of 1 m according to *Bernie et al.* [2005] in order to properly produce the majority of diurnal variability. Using a model that produces a better estimation of the diurnal warming gradients would be useful in order to understand whether the magnitude of the gradient is important in low wind speed regimes. Longer simulations would also be helpful in order to understand the role of the weather feedbacks on the longer-term mean wind, pressure, and heat flux changes in response to diurnal variability of SST.

The wind-diurnal SST coupling presented herein suggests that the role of atmospheric stability may be important in terms of vertical mixing transport of heat and momentum; we would be interested to know the significance of atmospheric stability in coupling SST-wind perturbations. This could be done via idealized simulations under varying wind speed conditions in order to understand whether the dominant forcing mechanisms change. These suggestions could provide great insight to the dynamics that control the SST-wind anomaly coupling on longer timescales.

BIBLIOGRAPHY

Aiyyer, A. R., and C. Thorncroft (2006), Climatology of vertical wind shear over the tropical atlantic, *J. Climate*, *19*(12), 2969–2983, doi:10.1175/JCLI3685.1.

Alexander, M. A., I. Bladé, M. Newman, J. R. Lanzante, N.-C. Lau, and J. D. Scott (2002), The atmospheric bridge: The influence of enso teleconnections on air-sea interaction over the global oceans, *J. Climate*, *15*(16), 2205–2231, doi:10.1175/1520-0442(2002)015¡2205:TABTIO¿2.0.CO;2.

Anderson, S. P. (2001), On the atmospheric boundary layer over the equatorial front*, *J. Climate*, *14*(7), 1688–1695, doi:10.1175/1520-0442(2001)014<1688:OTABLO>2.0.CO;2.

Back, L. E., and C. S. Bretherton (2009), On the relationship between SST gradients, boundary layer winds, and convergence over the tropical oceans, *J. Climate*, *22*, doi: 10.1175/2009jcli2392.1.

Bellenger, H., and J. Duvel (2009), An analysis of tropical ocean diurnal warm layers, *J. Climate*, *22*, doi:10.1175/2008JCLI2598.1.

Bernie, D., S. Woolnough, and J. Slingo (2005), Modeling diurnal and intraseasonal variability of the ocean mixed layer., *J. Climate*, *18*, 1190–1202, doi:10.1175/JCLI3319.1.

Bernie, D. J., E. Guilyardi, G. Madec, J. M. Slingo, and S. J. Woolnough (2007), Impact of resolving the diurnal cycle in an oceanatmosphere GCM. part 1: a diurnally forced OGCM, *Climate Dynamics*, *29*, doi:10.1007/s00382-007-0249-6.

Bourras, D., G. Reverdin, H. Giordani, and G. Caniaux (2004), Response of the atmospheric boundary layer to a mesoscale oceanic eddy in the northeast atlantic, *J. Geophys. Res.*, *109*(D18).

Brunke, M. A., X. Zeng, V. Misra, and A. Beljaars (2008), Integration of a prognostic sea surface skin temperature scheme into weather and climate models, *J. Geophys. Res.*, *113*(D21), doi: 10.1029/2008JD010607.

Chelton, D. B., and F. J. Wentz (2005), Global microwave satellite observations of sea surface temperature for numerical weather prediction and climate research, *Bull. Amer. Meteor. Soc.*, *86*, doi:10.1175/BAMS-86-8-1097.

Chelton, D. B., S. K. Esbensen, M. G. Schlax, N. Thum, M. H. Freilich, F. J. Wentz, C. L. Gentemann, M. J. McPhaden, and P. S. Schopf (2001), Observations of coupling between surface wind stress and sea surface temperature in the eastern tropical pacific, *J. Climate*, *14*(7), 1479–1498.

Chelton, D. B., M. G. Schlax, M. H. Freilich, and R. F. Milliff (2004), Satellite measurements reveal persistent small-scale features in ocean winds., *Science*, *303*(5660), 978–983, doi: 10.1126/science.1091901.

Chelton, D. B., M. G. Schlax, and R. M. Samelson (2007), Summertime coupling between sea surface temperature and wind stress in the california current system., *J. Phys. Oceanogr.*, *37*(3).

Chen, S. S., and R. A. Houze (1997), Diurnal variation and lifecycle of deep convective systems over the tropical pacific warm pool, *Q. J. R. Meteorol. Soc.*, doi:10.1002/qj.49712353806.

Clarke, A. (2008), *An Introduction to the Dynamics of El Nino & the Southern Oscillation*, Elsevier Science, Massachusetts.

Clayson, C. A., and A. S. Bogdanoff (2013), The effect of diurnal sea surface temperature warming on climatological AirSea fluxes, *J. Climate*, *26*, doi:10.1175/JCLI-D-12-00062.1.

Clayson, C. A., and D. Weitlich (2007), Variability of tropical diurnal sea surface temperature*, *J. Climate*, *20*, doi:10.1175/JCLI3999.1.

Danabasoglu, G., W. G. Large, J. J. Tribbia, P. R. Gent, B. P. Briegleb, and J. C. McWilliams (2006), Diurnal coupling in the tropical oceans of ccsm3, *J. Climate*, *19*(11), 2347–2365.

Donlon, C., et al. (2007), The global ocean data assimilation experiment high-resolution sea surface temperature pilot project, *Bull. Am. Meteorol. Soc.*, *88*, doi:10.1175/BAMS-88-8-1197.

Dudhia, J. (1989), Numerical study of convection observed during the winter monsoon experiment using a mesoscale two-dimensional model, *J. Atmos. Sci.*, *46*(20), 3077–3107.

Eichler, T., and W. Higgins (2006), Climatology and enso-related variability of north american extratropical cyclone activity, *J. Climate*, *19*(10), 2076–2093.

Fairall, C. W., E. F. Bradley, D. P. Rogers, J. B. Edson, and G. S. Young (1996a), Bulk parameterization of air-sea fluxes for tropical ocean-global atmosphere coupled-ocean atmosphere response experiment, *J. Geophys. Res.*, *101*(C2), 3747–3764.

Fairall, C. W., E. F. Bradley, J. S. Godfrey, G. A. Wick, J. B. Edson, and G. S. Young (1996b), Cool-skin and warm-layer effects on sea surface temperature, *J. Geophys. Res.*, *101*(C1), 1295–1308, doi:10.1029/95JC03190.

Filipiak, M., C. Merchant, H. Kettle, and L. P. Borgne (2012), An empirical model for the statistics of sea surface diurnal warming, *Ocean Science*, *8*(2), 197–209.

Gentemann, C. L. (2003), Diurnal signals in satellite sea surface temperature measurements, *Geophys. Res. Lett.*, *30*, doi:10.1029/2002GL016291.

Gentemann, C. L., and P. J. Minnett (2008), Radiometric measurements of ocean surface thermal variability, *J. Geophys. Res.*, *113*, doi:10.1029/2007JC004540.

Gentemann, C. L., P. J. Minnett, P. L. Borgne, and C. J. Merchant (2008), Multi-satellite measurements of large diurnal warming events, *Geophys. Res. Lett.*, *35*, doi:10.1029/2008GL035730.

Gentemann, C. L., P. J. Minnett, and B. Ward (2009), Profiles of ocean surface heating (POSH): a new model of upper ocean diurnal warming, *J. Geophys. Res.*, *114*, doi: 10.1029/2008JC004825.

Goldenberg, S. B., and L. J. Shapiro (1996), Physical mechanisms for the association of el nino and west african rainfall with atlantic major hurricane activity, *J. Climate*, *9*(6), 1169–1187.

Grenier, H., and C. S. Bretherton (2001), A moist pbl parameterization for large-scale models and its application to subtropical cloud-topped marine boundary layers, *Mon. Wea. Rev.*, *129*(3), 357–377.

Hashizume, H., S.-P. Xie, W. T. Liu, and K. Takeuchi (2001), Local and remote atmospheric response to tropical instability waves: A global view from space, *J. Geophys. Res.*, *106*(D10), 10,173–10,185.

Hashizume, H., S. Xie, M. Fujiwara, M. Shiotani, T. Watanabe, Y. Tanimoto, T. W. Liu, and K. Takeuchi (2002), Direct observations of atmospheric boundary layer response to SST variations associated with tropical instability waves over the eastern equatorial pacific*, *J. Climate*, *15*(23), 3379–3393.

Hong, S.-Y., and J.-O. J. Lim (2006), The wrf single-moment 6-class microphysics scheme (wsm6), *J. Korean Meteor. Soc*, *42*(2), 129–151.

Inness, P. M., J. M. Slingo, E. Guilyardi, and J. Cole (2003), Simulation of the madden-julian oscillation in a coupled general circulation model. part ii: The role of the basic state, *J. Climate*, *16*(3), 365–382.

Kain, J. S. (2004), The kain-fritsch convective parameterization: an update, *J. Applied Meteor.*, *43*(1), 170–181.

Kawai, Y., and A. Wada (2007), Diurnal sea surface temperature variation and its impact on the atmosphere and ocean: A review, *J. of Oceanogr.*, *63*(5), 721–744, doi:10.1007/s10872-007-0063-0.

Kennedy, J. J., P. Brohan, and S. F. B. Tett (2007), A global climatology of the diurnal variations in sea-surface temperature and implications for MSU temperature trends, *Geophys. Res. Lett.*, *34*, doi:10.1029/2006GL028920.

Kilpatrick, T., N. Schneider, and B. Qiu (2014), Boundary layer convergence induced by strong winds across a midlatitude SST front*, *J. Climate*, *27*(4), 1698–1718.

Lambaerts, J., G. Lapeyre, R. Plougonven, and P. Klein (2013), Atmospheric response to sea surface temperature mesoscale structures, *J. Geophys. Res.*, *118*(17), 9611–9621.

Lee-Thorp, A., M. Rouault, and J. Lutjeharms (1999), Moisture uptake in the boundary layer above the agulhas current: A case study, *J. Geophys. Res.*, *104*(C1), 1423–1430.

Lindzen, R. S., and S. Nigam (1987), On the role of sea surface temperature gradients in forcing low-level winds and convergence in the tropics, *J. Atmos. Sci.*, *44*(17), 2418–2436.

Liu, T. W., X. Xie, P. S. Polito, S. Xie, and H. Hashizume (2000), Atmospheric manifestation of tropical instability wave observed by QuikSCAT and tropical rain measuring mission, *Geophys. Res. Lett.*, *27*(16), 2545–2548, doi:10.1029/2000GL011545.

Maturi, E., A. Harris, C. Merchant, J. Mittaz, B. Potash, W. Meng, and J. Sapper (2008), Noaa's sea surface temperature products from operational geostationary satellites, *Bull. Amer. Meteor. Soc.*, *89*(12), 1877.

Merchant, C. J., M. J. Filipiak, P. L. Borgne, H. Roquet, E. Autret, J. Piollé, and S. Lavender (2008), Diurnal warm-layer events in the western mediterranean and european shelf seas, *Geophys. Res. Lett.*, *35*, doi:10.1029/2007GL033071.

Minobe, S., A. Kuwano-Yoshida, N. Komori, S.-P. Xie, and R. J. Small (2008), Influence of the gulf stream on the troposphere, *Nature*, *452*(7184), 206–209.

Mlawer, E., and S. Clough (1997), On the extension of rapid radiative transfer model to the shortwave region, in *Proceedings of the 6th Atmospheric Radiation Measurement (ARM) Science Team Meeting, US Department of Energy, CONF-9603149*.

Noh, Y., W. Cheon, S. Hong, and S. Raasch (2003), Improvement of the k-profile model for the planetary boundary layer based on large eddy simulation data, *Boundary-layer meteorology*, *107*(2), 401–427.

Noh, Y., E. Lee, D. Kim, S. Hong, M. Kim, and M. Ou (2011), Prediction of the diurnal warming of sea surface temperature using an atmosphere-ocean mixed layer coupled model, *J. Geophys. Res.*, *116*, doi:10.1029/2011JC006970.

O'Neill, L. W., S. K. Esbensen, N. Thum, R. M. Samelson, and D. B. Chelton (2010), Dynamical analysis of the boundary layer and surface wind responses to mesoscale SST perturbations, *J. Climate*, *23*(3), 559–581.

O'Neill, L. (2012), Wind speed and stability effects on coupling between surface wind stress and SST observed from buoys and satellite, *J. Climate*, *25*(5), 1544–1569.

Park, K., and P. C. Cornillon (2002), Stability-induced modification of sea surface winds over gulf stream rings, *Geophys. Res. Lett.*, *29*(24).

Pielke, R. (2013), *Mesoscale Meteorological Modeling*, International Geophysics, 3 ed., Academic Press, Massachusetts.

Pimentel, S., K. Haines, and N. K. Nichols (2008), Modeling the diurnal variability of sea surface temperatures, *J. Geophys. Res.*, *113*, doi:10.1029/2007JC004607.

Price, J. F., R. A. Weller, and R. Pinkel (1986), Diurnal cycling: Observations and models of the upper ocean response to diurnal heating, cooling, and wind mixing, *J. Geophys. Res.*, *91*(C7), doi:10.1029/JC091iC07p08411.

Schiller, A., and J. Godfrey (2005), A diagnostic model of the diurnal cycle of sea surface temperature for use in coupled ocean-atmosphere models, *J. Geophys. Res.*, *110*(C11).

Shinoda, T. (2005), Impact of the diurnal cycle of solar radiation on intraseasonal sst variability in the western equatorial pacific, *J. Climate*, *18*(14), 2628–2636.

Shinoda, T., and H. H. Hendon (1998), Mixed layer modeling of intraseasonal variability in the tropical western pacific and indian oceans, *J. Climate*, *11*(10), 2668–2685.

Skamarock, W., J. Klemp, J. Dudhia, D. Gill, D. Barker, M. Duda, X. Huang, W. Wang, and J. Powers (2008), A description of the advanced research wrf version 3, ncar technical note, mesoscale and microscale meteorology division, *National Center for Atmospheric Research, Boulder, Colorado, USA*.

Small, R., S. Xie, L. ONeill, H. Seo, Q. Song, P. Cornillon, M. Spall, S. Minobe, et al. (2008), Air–sea interaction over ocean fronts and eddies, *Dyn. Atmos. Oceans*, *45*(3), 274–319.

Soloviev, A., and R. Lukas (1997), Observation of large diurnal warming events in the near-surface layer of the western equatorial pacific warm pool, *Deep-Sea Res. I*, *44*, 1055–1076.

Soloviev, A., and R. Lukas (2006), *The Near-Surface Layer of the Ocean: Structure, Dynamics and Applications*, Atmospheric and Oceanographic Sciences Library, Springer, 3300 AA Dordrecht, The Netherlands.

Song, Q., P. Cornillon, and T. Hara (2006), Surface wind response to oceanic fronts, *J. Geophys. Res.*, *111*(C12), doi:10.1029/2006JC003680.

Song, Q., D. Chelton, S. Esbensen, and N. Thum (2009), Coupling between sea surface temperature and low-level winds in mesoscale numerical models, *J. Climate*, *22*, 146–164, doi: 10.1175/2008JCLI2488.1.

Stramma, L., P. Cornillon, and R. Weller (1986), Large diurnal sea surface temperature variability: Satellite and in situ measurements, *J. Phys. Oceanogr.*, *16*(5), 827–837, doi:10.1175/1520-0485(1986)016<0827:LDSSTV>2.0.CO;2.

Stuart-Menteth, A. C. (2003), A global study of diurnal warming using satellite-derived sea surface temperature, *J. of Geophys. Res.*, *108*, doi:10.1029/2002JC001534.

Sverdrup, H. U., M. W. Johnson, and R. H. Fleming (1942), *The oceans, their physics, chemistry, and general biology*, Prentice-Hall, New York.

Sweet, W., R. Fett, and J. Kerling (1981), Air-sea interaction effects in the lower troposphere across the north wall of the Gulf Stream, *Mon. Wea. Rev.*, *109*, 1042–1052, doi:10.1175/1520-0493(1981)109<1042:ASIEIT>2.0.CO;2.

Takaya, Y., J.-R. Bidlot, A. Beljaars, and P. A. Janssen (2010), Refinements to a prognostic scheme of skin sea surface temperature, *J. Geophys. Res.*, *115*(C6), doi:10.1029/2009JC005985.

Wai, M. M.-K., and S. A. Stage (1989), Dynamical analyses of marine atmospheric boundary layer structure near the gulf stream oceanic front, *Q.J.R. Meteorol. Soc.*, *115*(485), 29–44, doi:10.1002/qj.49711548503.

Wallace, J. M., T. Mitchell, and C. Deser (1989), The influence of sea-surface temperature on surface wind in the eastern equatorial pacific: seasonal and interannual variability, *J. Climate*, *2*(12), 1492–1499, doi:10.1175/1520-0442(1989)002<1492:TIOSST>2.0.CO;2.

Wang, Z., and A. M. Duan (2012), A new ocean mixed-layer model coupled into WRF, *Atmos. Oceanic Sci. Lett.*, *5*(3), 170–175, doi:10.1080/16742834.2012.11446988.

Ward, B. (2006), Near-surface ocean temperature, *J. Geophys. Res.*, *111*(C2), doi: 10.1029/2004JC002689.

Webster, P. J., C. A. A. Clayson, and J. A. Curry (1996), Clouds, radiation, and the diurnal cycle of sea surface temperature in the tropical western pacific, *J. Climate*, *9*(8), doi:10.1175/1520-0442(1996)009¡1712:CRATDC¿2.0.CO;2.

Wei, L., Y. Rucong, L. Hailong, and Y. Yongqiang (2001), Impacts of diurnal cycle of SST on the intraseasonal variation of surface heat flux over the Western Pacific Warm Pool, *Adv. Atmos. Sci.*, *18*(5).

Weihs, R. R., and M. A. Bourassa (2014), Modeled diurnally varying sea surface temperatures and their influence on surface heat fluxes, *J. Geophys. Res.*, *119*(7), 4101–4123, doi: 10.1002/2013JC009489.

Wick, G. A., J. C. Ohlmann, C. W. Fairall, and A. T. Jessup (2005), Improved oceanic cool-skin corrections using a refined solar penetration model, *J. Phys. Oceanogr.*, *35*(11), 1986–1996, doi:10.1175/JPO2803.1.

Woolnough, S., J. Slingo, and B. Hoskins (2000), The relationship between convection and sea surface temperature on intraseasonal timescales, *J. Climate*, *13*(12), 2086–2014, doi: 10.1175/1520-0442(2000)013<2086:TRBCAS>2.0.CO;2.

Xie, S.-P. (2004), Satellite observations of cool ocean-atmosphere interaction*, *Bull. Amer. Meteor. Soc.*, *85*(2), 195, doi:10.1175/BAMS-85-2-195.

Zeng, X., and A. Beljaars (2005), A prognostic scheme of sea surface skin temperature for modeling and data assimilation, *Geophys. Res. Lett*, *32*(14), doi:10.1029/2005GL023030.

BIOGRAPHICAL SKETCH

Rachel Weihs was born and raised in Boulder, Colorado and moved to Sarasota, Florida in 1995. She received a music scholarship to attend Florida State University in 2003 to pursue a Bachelor of Art's degree in Music Education. However, her interest in weather, stemming from personal experience of weather extremes while growing up, influenced her to switch her degree to meteorology soon thereafter. She has earned a Bachelor's degree in meteorology in 2008 and a Master's degree in meteorology in 2012 under the advisement of Dr. Mark Bourassa.

During her graduate career, Rachel participated in several opportunities of leadership while at Florida State; in 2010-2013, she was part of a NASA-funded program to design and facilitate a professional development workshop series on global and regional climate change for middle school teachers. She was also on the executive board for the Graduate Women in Science student organization from 2015-2016 and was elected as the meteorology Graduate Student Representative for the Department of Earth, Ocean, and Atmospheric Science from 2014-2015. She was inducted into the meteorology Chi Epsilon Pi honor society and served as Vice President in 2009.

In the summer of 2015, Rachel participated in the summer internship program at the Jet Propulsion Laboratory in Pasadena, CA. There, she was mentored by Jorge Vazquez and Dimitris Menemenlis, experts in the sea surface temperature and ocean modeling community. The experience she had at JPL was instrumental in focusing her dissertation research. After spending 10+ arduous years in Tallahassee, Rachel will be heading to Scripps Institution of Oceanography in San Diego, CA as a Postdoc where she will be studying the representation of atmospheric river events in the Weather and Research Forecasting model over the eastern Pacific Ocean.